Article

Cell Chemical Biology

Polynuclear Ruthenium Amines Inhibit K_{2P} Channels via a "Finger in the Dam" Mechanism

Graphical Abstract

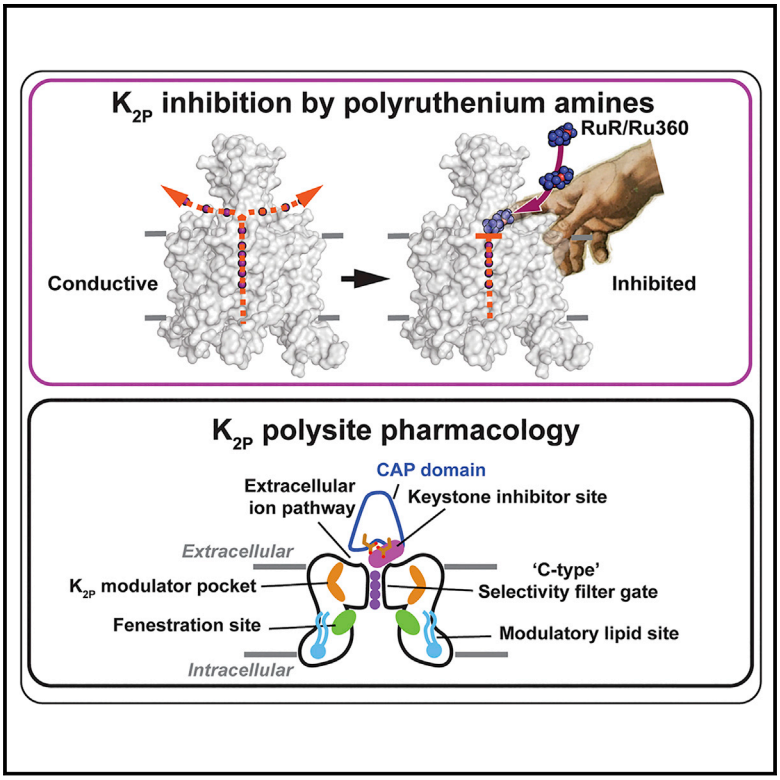

Highlights

- Polynuclear ruthenium amines bind the CAP domain Keystone inhibitor site
- Electrostatics and direct side chain coordination contribute to RuR and Ru360 binding
- RuR and Ru360 prevent ion flow by a "finger in the dam" blockade
- Structure-based design creates RuR super-responder K_{2P}s

Authors

Lianne Pope, Marco Lolicato, Daniel L. Minor, Jr.

Correspondence

daniel.minor@ucsf.edu

In Brief

Polynuclear ruthenium amines inhibit diverse ion channel classes. Pope et al. describe the structural basis of K_{2P} potassium channel inhibition by ruthenium red (RuR) and Ru360, defining a "finger in the dam" mechanism highlighting K_{2P} polysite pharmacology and providing a framework for understanding polynuclear amine recognition.

Pope et al., 2020, Cell Chemical Biology *27*, 511–524
May 21, 2020
https://doi.org/10.1016/j.chembiol.2020.01.011

CellPress

Cell Chemical Biology

CellPress

Article

Polynuclear Ruthenium Amines Inhibit K_{2P} Channels via a "Finger in the Dam" Mechanism

Lianne Pope,[1] Marco Lolicato,[1,6] and Daniel L. Minor, Jr.[1,2,3,4,5,7,*]
[1]Cardiovascular Research Institute, University of California, San Francisco, CA 93858-2330, USA
[2]Departments of Biochemistry and Biophysics, and Cellular and Molecular Pharmacology, University of California, San Francisco, CA 93858-2330, USA
[3]California Institute for Quantitative Biomedical Research, University of California, San Francisco, CA 93858-2330, USA
[4]Kavli Institute for Fundamental Neuroscience, University of California, San Francisco, CA 93858-2330, USA
[5]Molecular Biophysics and Integrated Bio-imaging Division, Lawrence Berkeley National Laboratory, Berkeley, CA 94720, USA
[6]Present address: Department of Molecular Medicine, University of Pavia, Pavia, Italy
[7]Lead Contact
*Correspondence: daniel.minor@ucsf.edu
https://doi.org/10.1016/j.chembiol.2020.01.011

SUMMARY

The trinuclear ruthenium amine ruthenium red (RuR) inhibits diverse ion channels, including K_{2P} potassium channels, TRPs, the calcium uniporter, CALHMs, ryanodine receptors, and Piezos. Despite this extraordinary array, there is limited information for how RuR engages targets. Here, using X-ray crystallographic and electrophysiological studies of an RuR-sensitive K_{2P}, K_{2P}2.1 (TREK-1) I110D, we show that RuR acts by binding an acidic residue pair comprising the "Keystone inhibitor site" under the K_{2P} CAP domain archway above the channel pore. We further establish that Ru360, a dinuclear ruthenium amine not known to affect K_{2P}s, inhibits RuR-sensitive K_{2P}s using the same mechanism. Structural knowledge enabled a generalizable design strategy for creating K_{2P} RuR "super-responders" having nanomolar sensitivity. Together, the data define a "finger in the dam" inhibition mechanism acting at a novel K_{2P} inhibitor binding site. These findings highlight the polysite nature of K_{2P} pharmacology and provide a new framework for K_{2P} inhibitor development.

INTRODUCTION

Ruthenium red (RuR) (Fletcher et al., 1961) (Figure 1A) is a trinuclear oxo-bridged ruthenium amine polycation with many biological applications (Clarke, 2002), including a ~50-year legacy of use as an inhibitor of diverse ion channels, such as select members of the K_{2P} (KCNK) family (Braun et al., 2015; Czirjak and Enyedi, 2003; Gonzalez et al., 2013; Musset et al., 2006), numerous TRP channels (Arif Pavel et al., 2016; Caterina et al., 1997, 1999; Guler et al., 2002; Story et al., 2003; Strotmann et al., 2000; Voets et al., 2002, 2004), the mitochondrial calcium uniporter (MCU) (Chaudhuri et al., 2013; Kirichok et al., 2004; Moore, 1971; Rahamimoff and Alnaes, 1973), CALHM calcium channels (Choi et al., 2019; Dreses-Werringloer et al., 2013; Ma et al., 2012), ryanodine receptors (Ma, 1993; Smith et al., 1988), and Piezo channels (Coste et al., 2012; Zhao et al., 2016). Despite this remarkably wide range of ion channel targets and the recent boom in ion channel structural biology, structural understanding of how RuR acts on any ion channel is limited to a recent cryoelectron microscopy study of the CALHM2 channel that provides few molecular details regarding the coordination chemistry that underlies RuR binding (Choi et al., 2019). In the case of K_{2P}s, functional studies have established that a negatively charged residue at the base of the K_{2P} extracellular dimerization domain that forms an archway over the channel pore, the CAP domain, comprises a key RuR sensitivity determinant in the natively RuR-sensitive channels K_{2P}9.1 (TASK-3) (Czirjak and Enyedi, 2003; Gonzalez et al., 2013; Musset et al., 2006) and K_{2P}10.1 (TREK-2) (Braun et al., 2015). Furthermore, installation of a negatively charged amino acid at the equivalent CAP domain site in a non-RuR-sensitive channel is sufficient to confer RuR sensitivity (Braun et al., 2015). The archway above the selectivity filter extracellular mouth made by the K_{2P} CAP domain creates a pair of water-filled portals, the extracellular ion pathway (EIP), through which ions exit the channel under physiological conditions (Brohawn et al., 2012; Dong et al., 2015; Lolicato et al., 2017; Miller and Long, 2012). Although the EIP has been proposed as the site of RuR action (Braun et al., 2015; Gonzalez et al., 2013), the mechanism by which RuR inhibits K_{2P}s remains unresolved and to date there is no direct structural evidence indicating that the EIP can be targeted by RuR or any other class of small-molecule or protein-based inhibitors.

K_{2P}s produce an outward "leak" potassium current that plays a critical role in stabilizing the resting membrane potential of diverse cell types in the nervous, cardiovascular, and immune systems (Enyedi and Czirjak, 2010; Feliciangeli et al., 2014; Renigunta et al., 2015). There are 15 K_{2P} subtypes comprising 6 subfamilies in which the channel monomers assemble into dimers wherein each subunit contributes two conserved pore-forming domains to make the channel pore (Brohawn et al., 2012; Dong et al., 2015; Feliciangeli et al., 2014; Lolicato et al., 2017; Miller and Long, 2012; Rödström et al., 2019). A range of physical and chemical signals control K_{2P} function (Enyedi and Czirjak, 2010; Feliciangeli et al., 2014; Renigunta et al., 2015)

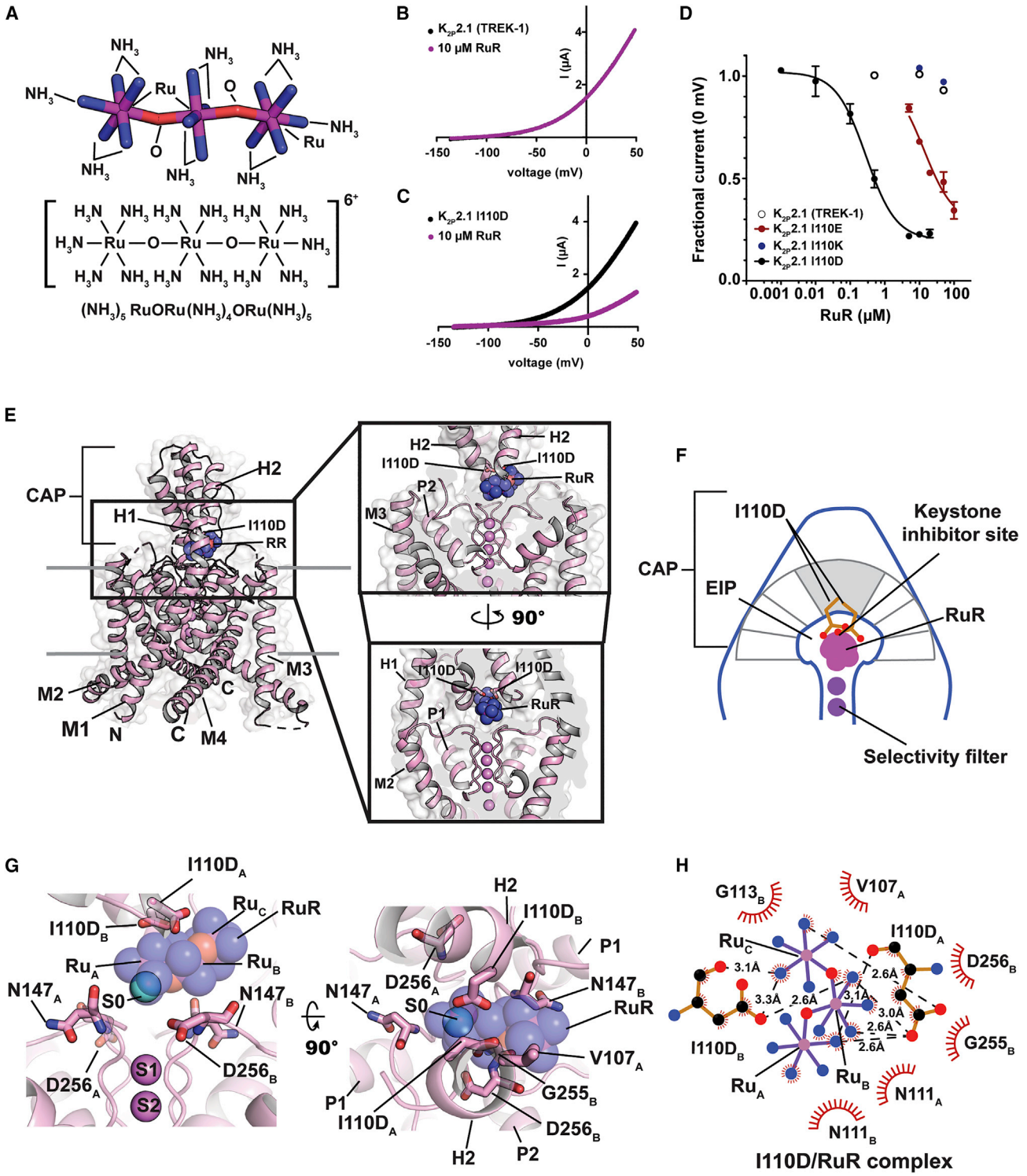

Figure 1. Functional and Structural Analysis of the K_{2P}2.1 I110D:RuR Complex

(A) Ruthenium red (RuR) structure.

(B and C) Exemplar TEVC recordings of (B) K_{2P}2.1 (TREK-1) and (C) K_{2P}2.1 I110D responses to 10 μM RuR (magenta).

(D) Dose-response curves for K_{2P}2.1 (TREK-1) (open white circles), K_{2P}2.1 I110D (black), K_{2P}2.1 I110E (red), and K_{2P}2.1 I110K (dark blue) to RuR. Error bars are SEM.

(E) Structure of the K_{2P}2.1 I110D:RuR complex. Inset shows the location of the RuR binding site. I110D is shown as sticks.

(legend continued on next page)

Table 1. IC_{50} Values for RuR and Ru360

Inhibitor		Construct	EC_{50} (μM)	n
RuR	K_{2P}2.1 (TREK-1)	K_{2P}2.1 (TREK-1)	>100	3
		K_{2P}2.1 I110D	0.287 ± 0.054	3
		K_{2P}2.1 I110E	13.6 ± 2.7	3
		K_{2P}2.1 I110K	>100	
		K_{2P}2.1 I110D/G137I	0.154 ± 0.023	3
		K_{2P}2.1 I110D + 50 μM ML335	0.173 ± 0.021	3
		K_{2P}2.1 N147D	47.7 ± 6.3[a]	2
		K_{2P}2.1 N147E	0.0733 ± 0.0165	3
		K_{2P}2.1 I110D/N147D	0.0127 ± 0.0023	3
		K_{2P}2.1 I110D/N147E	0.0126 ± 0.0034	3
	Other K_{2P}s	K_{2P}10.1 (TREK-2) [D135][b]	0.23 ± 0.06 (Braun et al., 2015)	
		K_{2P}9.1 (TASK-3) [E70][b]	0.114 ± 0.021	3
Ru360	K_{2P}2.1 (TREK-1)	K_{2P}2.1 (TREK-1)	>100	3
		K_{2P}2.1 I110D	11.3 ± 1.8	3
	Other K_{2P}s	K_{2P}10.1 (TREK-2) [D135][b]	2.8 ± 1.2	3
		K_{2P9}.1 (TASK-3) [E70][b]	15.6 ± 2.7	3

n, number of oocytes.
Errors are SEM.
[a]Lower bound constrained to 0.2.
[b]Residue at the K_{2P}2.1 (TREK-1) I110D equivalent position.

and various K_{2P} subtypes have emerging roles in a multitude of physiological responses and pathological conditions, such as action potential propagation in myelinated axons (Brohawn et al., 2019; Kanda et al., 2019), anesthetic responses (Heurteaux et al., 2004; Lazarenko et al., 2010), microglial surveillance (Madry et al., 2018), sleep duration (Yoshida et al., 2018), pain (Alloui et al., 2006; Devilliers et al., 2013; Vivier et al., 2017), arrhythmia (Decher et al., 2017), ischemia (Heurteaux et al., 2004; Laigle et al., 2012; Wu et al., 2013), cardiac fibrosis (Abraham et al., 2018), depression (Heurteaux et al., 2006), migraine (Royal et al., 2019), intraocular pressure regulation (Yarishkin et al., 2018), and pulmonary hypertension (Lambert et al., 2018). Although there have been recent advances in identifying new K_{2P} modulators (Bagriantsev et al., 2013; Lolicato et al., 2017; Pope et al., 2018; Su et al., 2016; Tian et al., 2019; Vivier et al., 2017; Wright et al., 2019) and in defining key structural aspects of K_{2P} channel pharmacology (Dong et al., 2015; Lolicato et al., 2017; Schewe et al., 2019), as is the case with many ion channel classes, pharmacological agents targeting K_{2P}s remain poorly developed and limit the ability to probe K_{2P} mechanism and biological functions (Sterbuleac, 2019).

Here, we present X-ray crystal structures of a K_{2P}2.1 (TREK-1) mutant bearing a single change at the site that controls K_{2P} channel RuR sensitivity, K_{2P}2.1 I110D, alone and complexed with two different polynuclear ruthenium amines, RuR and the dinuclear ruthenium amine, Ru360 (Ying et al., 1991), an inhibitor of the MCU (Baughman et al., 2011; Kirichok et al., 2004; Oxenoid et al., 2016) not previously known to affect potassium channels. The structures show that the negatively charged residues at position 110 comprise the "Keystone inhibitor site" on the ceiling of the CAP domain archway to which positively charged RuR and Ru360 bind through ionic interactions. This interaction holds the polybasic compounds directly over the mouth of the channel pore, blocks one EIP arm, and prevents channel function. Functional studies corroborated by a crystal structure of K_{2P}2.1 I110D bound simultaneously to RuR and a small-molecule activator of the channel selectivity filter "C-type gate," ML335 (Lolicato et al., 2017), establish that polynuclear ruthenium amine inhibition of K_{2P}s is unaffected by C-type gate activation. Using molecular recognition principles derived from the structures of the K_{2P}:RuR and K_{2P}:Ru360 complexes, we demonstrate a general design strategy for endowing any K_{2P} channel with nanomolar RuR sensitivity. Our work establishes that polynuclear ruthenium compounds act through a "finger in the dam" mechanism to inhibit K_{2P} function by binding under the CAP domain archway at the Keystone inhibitor site and blocking the selectivity filter pore. The structural definition of this new modulatory site demonstrates the importance of electronegativity and specific side-chain geometry for polynuclear amine molecular recognition, defines a new small-molecule binding site that augments the rich, polysite pharmacology of K_{2P} modulation, and opens a path for targeting the Keystone inhibitor site and EIP for the development of new K_{2P} modulators.

RESULTS

A Single Site in the K_{2P} CAP Domain Confers RuR Sensitivity

K_{2P}2.1 (TREK-1) is the founding member of the thermo- and mechanosensitive subgroup of K_{2P}s (Douguet and Honore, 2019; Feliciangeli et al., 2014). Although this channel is resistant to RuR inhibition (Figures 1B and 1D; Table 1) (Braun et al., 2015), two-electrode voltage-clamp (TEVC) recordings in *Xenopus* oocytes of outward current inhibition by RuR under physiological ionic conditions showed that installation of a point mutation I110D at the base of the K_{2P}2.1 (TREK-1) CAP domain conferred sub-micromolar RuR sensitivity to K_{2P}2.1 (TREK-1) (IC_{50} = 0.287 ± 0.054 μM) (Figures 1C and 1D; Table 1). This inhibition followed a 1:1 RuR:channel stoichiometry, in agreement with K_{2P} studies using other recording protocols (Braun et al., 2015; Czirjak and Enyedi, 2003), and validates previous studies showing that this point mutant renders K_{2P}2.1 (TREK-1) sensitive to RuR (Braun et al., 2015). Importantly, the response of K_{2P}2.1

(F) Cartoon depicting the Keystone inhibitor site. View is from the lower panel of (E). The archway formed by the CAP is shown in gray. The Keystone position is shaded.
(G) Close up view of K_{2P}2.1 I110D:RuR interactions. S0 ion (cyan) from the K_{2P}2.1 I110D structure is indicated. Subscripts indicate chain A and chain B residues. RuR is shown in space filling in (E) and (G).
(H) LigPLOT (Wallace et al., 1995) diagram of K_{2P}2.1 I110D:RuR interactions showing ionic interactions (dashed lines) and van der Waals contacts (red) ≤5 Å.
See also Figures S1 and S2 and Tables S1 and S2.

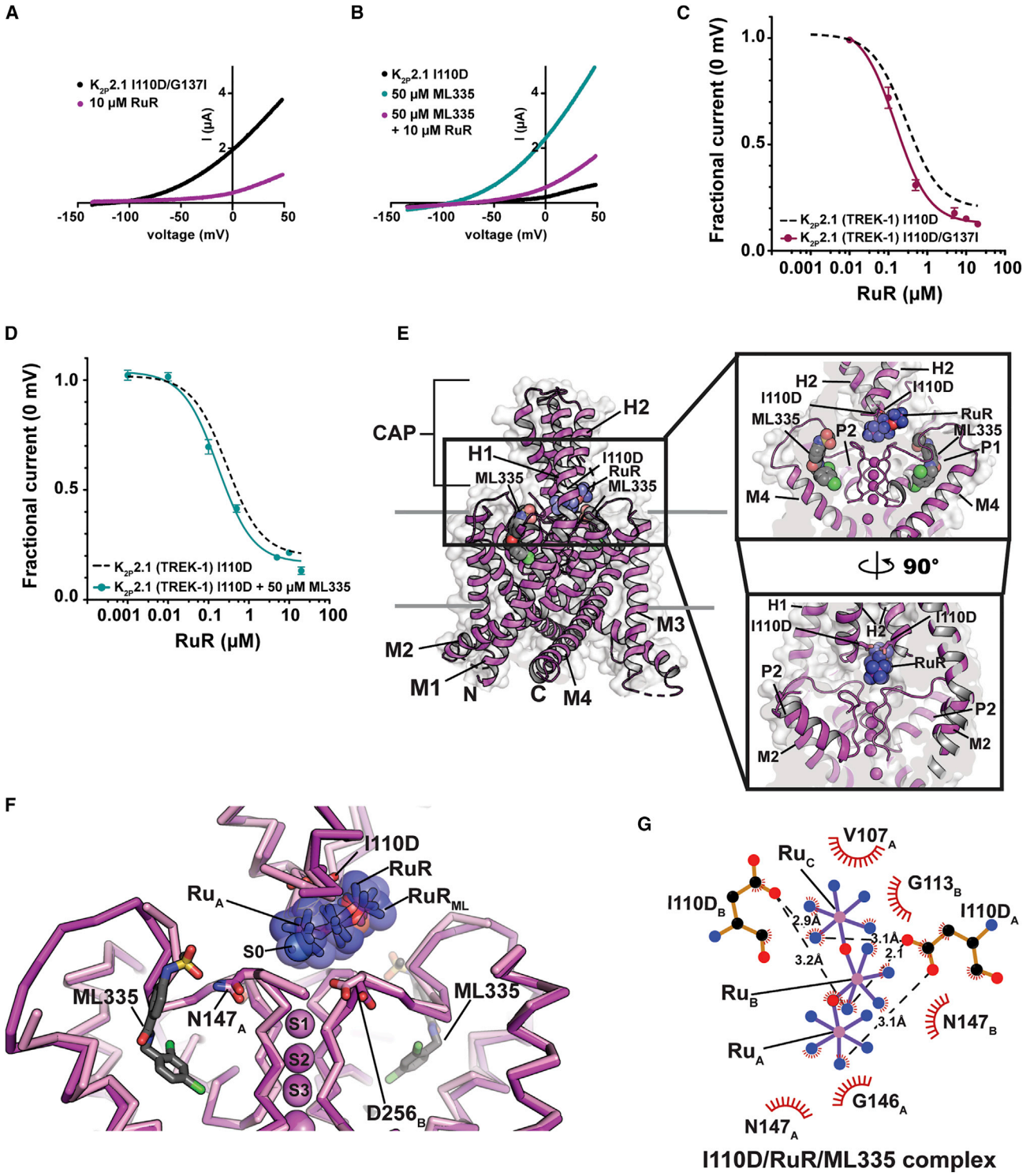

Figure 2. Functional and Structural Analysis of C-type Gate Activated K_{2P}2.1 I110D:RuR Complexes

(A and B) Exemplar TEVC recordings of (A) K_{2P}2.1 I110D/G137I (black) and in the presence of 10 μM RuR (magenta), and (B) K_{2P}2.1 I110D alone (black) in the presence of 50 μM ML335 (cyan), and in the presence of 50 μM ML335 + 10 μM RuR (magenta).

(C and D) RuR dose-response curves for (C) K_{2P}2.1 I110D/G137I (magenta) and (D) K_{2P}2.1 I110D in the presence of 50 μM ML335 (cyan). Dashed lines show RuR response of K_{2P}2.1 I110D from Figure 1D. Error bars are SEM.

(E) Structure of the K_{2P}2.1 I110D:ML335 RuR complex. Inset shows the location of the RuR binding site. I110D is shown as sticks. ML335 (gray) is shown as space filling.

(legend continued on next page)

I110D to RuR matched that of the closely related, natively RuR-sensitive K_{2P}10.1 (TREK-2) (Braun et al., 2015), in which there are native aspartate residues at the K_{2P}2.1 Ile110 analogous site (Figures 1D and S1A; Table 1) (IC_{50} = 0.287 ± 0.054 and 0.23 ± 0.06 μM for K_{2P}2.1 I110D and K_{2P}10.1 (TREK-2) [Braun et al., 2015], respectively), suggesting that the I110D change to K_{2P}2.1 (TREK-1) captures the essence of the requirements for RuR inhibition.

Because another natively RuR-sensitive K_{2P}, K_{2P}9.1 (TASK-3), has a glutamate at the K_{2P}2.1 I110D equivalent site (Figure S1A) that is essential for its RuR response (Czirjak and Enyedi, 2003; Gonzalez et al., 2013; Musset et al., 2006), we asked whether I110E would also render K_{2P}2.1 (TREK-1) sensitive to RuR. Indeed, TEVC measurements showed that RuR inhibited K_{2P}2.1 I110E (IC_{50} = 13.6 ± 2.7 μM; Table 1) (Figures 1D and S1B; Table 1). RuR inhibition was ~50-fold weaker than that observed for K_{2P}2.1 I110D, indicating that the I110D and I110E changes are not equivalent even though both bear similar negative charges. Furthermore, introduction of a positively charged residue, K_{2P}2.1 I110K, yielded channels as insensitive to RuR as K_{2P}2.1 (TREK-1) (Figures 1D and S1C). RuR inhibition was essentially independent of voltage for K_{2P}2.1 I110D and K_{2P}2.1 I110E (Figures S1D–S1G), consistent with previous reports of RuR inhibition of other K_{2P}s (Czirjak and Enyedi, 2002). Together, these results provide key support for the idea that a negative charge at the K_{2P} CAP domain base is a crucial determinant of RuR inhibition of K_{2P}s (Braun et al., 2015; Czirjak and Enyedi, 2003; Gonzalez et al., 2013; Musset et al., 2006). Importantly, the observation of the ~50-fold difference between the RuR sensitivity of two essentially equivalently negatively charged residues in the same structural context, K_{2P}2.1 I110D and K_{2P}2.1 I110E (Figure 1D; Table 1) indicates that electrostatics is not the sole factor contributing to the RuR:channel interaction and points to a role for the detailed geometry of the interaction of the negatively charged residues with RuR.

Structural Definition of the K_{2P} RuR Binding Site

To understand how RuR inhibits K_{2P} channels, we determined the X-ray crystal structures of K_{2P}2.1 I110D alone and bound to RuR at resolutions of 3.40 and 3.40 Å, respectively (Table S1) on the background of the previously crystallized construct K_{2P}2.1 (TREK-1)$_{cryst}$ (Lolicato et al., 2017). Apart from the I110D change, the overall structure of K_{2P}2.1 I110D was essentially identical to K_{2P}2.1 (TREK-1)$_{cryst}$ (root-mean-square deviation [$RMSD_{C\alpha}$] = 0.575 Å) (Table S2). Importantly, K_{2P}2.1 I110D was structurally similar to the natively RuR-sensitive K_{2P}10.1 (TREK-2) (Dong et al., 2015) ($RMSD_{C\alpha}$ = 0.938 Å), especially in the neighborhood of K_{2P}10.1 (TREK-2) Asp140 (Figure S2A; Table S2), the residue that is fundamental to K_{2P}10.1 (TREK-2) RuR sensitivity (Braun et al., 2015). Hence, when taken together with the functional similarity to K_{2P}10.1 (TREK-2), the K_{2P}2.1 I110D:RuR complex should capture the essential elements that contribute to the RuR response of natively RuR-sensitive K_{2P}s.

The K_{2P}2.1 I110D:RuR complex structure shows that RuR binds under the CAP domain archway directly above the selectivity filter at a site we term the Keystone inhibitor site due to the location of the I110D residues at the peak of the CAP archway ceiling (Figures 1E, 1F, S2B, and S2C). RuR binds with a 1:1 stoichiometry to the channel that matches expectations from functional studies (Table 1) (Braun et al., 2015; Czirjak and Enyedi, 2002; 2003). To facilitate description of this and other RuR complexes, we designate the three RuR ruthenium amine centers as Ru_A, Ru_B, and Ru_C. RuR binds at an angle of ~45° relative to the CAP and selectivity filter in a pose that places one of the terminal ruthenium amine moieties, Ru_A, directly above the column of selectivity filter ions in a position that overlaps with the S0 ion site from the K_{2P}2.1 I110D structure (Figures 1G and S2B). The Ru_B and Ru_C moieties block one EIP arm (Figures 1E and 1G). Notably, the observed pose is very different from the previously proposed horizontal RuR binding pose in which the Ru_B moiety sits above the column of selectivity filter ions (Gonzalez et al., 2013). The I110D carboxylates coordinate RuR directly through electrostatic interactions with all three ruthenium amine moieties using a multipronged set of interactions (Figures 1G and 1H). Such direct coordination of RuR by multiple elements of the I110D ligands suggests why K_{2P}2.1 I110D and K_{2P}2.1 I110E have different magnitude RuR responses, as the extra methylene groups in K_{2P}2.1 I110E would not allow the same type of direct coordination observed for the smaller aspartate pair (Figure 1H). Besides direct electrostatic interactions, there are van der Waals contacts between Ru_C and the side chain of CAP residue Val107 from chain A, Ru_A and Ru_B with Asn111 from each chain of the dimer, Ru_A with Asp256 from chain B, and Ru_B with Gly255 from chain B. Apart from a slight reorientation of the I110D sidechains and CAP to accommodate RuR (Figure S2D; Video S1), there are only minor conformational changes with respect to the unbound K_{2P}2.1 I110D ($RMSD_{C\alpha}$ = 0.688 Å) (Table S2). Hence, RuR binds to an essentially pre-organized electronegative binding site at the CAP base.

K_{2P} RuR Binding Is Independent of C-type Gate Activation

Activation of the selectivity filter, C-type gate is central to K_{2P} function (Bagriantsev et al., 2011, 2012; Lolicato et al., 2017; Piechotta et al., 2011; Schewe et al., 2016) and diverse types of activators, including intracellular pH (Schewe et al., 2016), phosphatidylinositol 4,5-bisphosphate (PIP_2) (Schewe et al., 2016), pressure (Schewe et al., 2016), arachidonic acid (Schewe et al., 2016), small-molecule activators that target the K_{2P} modulator pocket (Lolicato et al., 2017), the activator BL-1249 (Pope et al., 2018), and the gain-of-function mutant G137I (Lolicato et al., 2017) have equivalent effects on C-type gate activation. Because RuR binds directly above the selectivity filter and overlaps with the S0 ion, we asked whether C-type gate activation by two representative means, the G137I mutation (Bagriantsev

(F) Superposition of RuR binding site from the K_{2P}2.1 I110D:RuR (pink) and K_{2P}2.1 I110D:ML335:RuR (magenta) RuR and RuR_{ML} indicate RuR from the K_{2P}2.1 I110D:RuR and K_{2P}2.1 I110D:ML335:RuR structures, respectively. ML335 is shown as sticks. Subscripts indicate chain A and chain B residues.
(G) LigPLOT (Wallace et al., 1995) diagram of K_{2P}2.1 I110D:RuR interactions from the K_{2P}2.1 I110D:ML335:RuR complex showing ionic interactions (dashed lines) and van der Waals contacts (red) ≤5 Å.
See also Figure S2 and Tables S1 and S2.

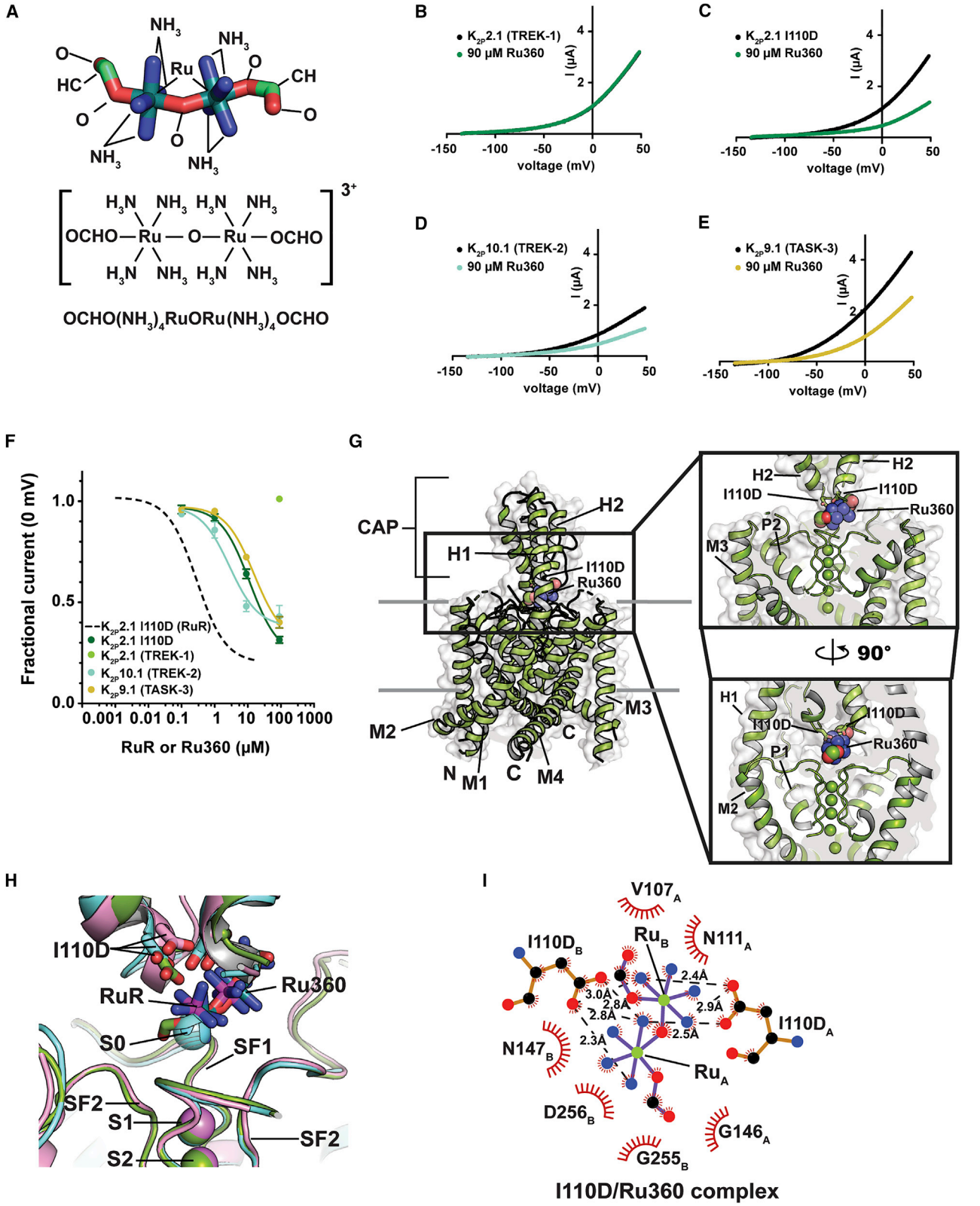

(legend on next page)

et al., 2012; Lolicato et al., 2014, 2017) or by a small-molecule activator, ML335 (Lolicato et al., 2017), would impact RuR inhibition of K_{2P}2.1 I110D (Figures 2A and 2B). TEVC experiments showed that RuR inhibits K_{2P}2.1 I110D/G137I with an IC_{50} (IC_{50} = 0.154 ± 0.023 μM) that is very similar to that for K_{2P}2.1 I110D, indicating that C-type gate activation does not influence RuR block of the channel (Figure 2C; Table 1).

Before assessing whether RuR inhibition was influenced by ML335 activation, we first measured the activation of K_{2P}2.1 I110D by ML335. The I110D change is >15 Å from the K_{2P} modulator pocket that forms the ML335 binding site and is not expected to impact ML335 activation. In line with these expectations, there was no difference in the response of K_{2P}2.1 I110D to ML335 activation relative to K_{2P}2.1 (TREK-1) ($EC_{50\ (ML335)}$ = 11.8 ± 2.3 and 14.3 ± 2.7 μM for K_{2P}2.1 I110D and K_{2P}2.1 (TREK-1) [Lolicato et al., 2017], respectively) (Figures S3A and S3B). Importantly, similar to the observations with the G137I C-type gate activation mutant, pharmacological C-type gate activation by saturating amounts of ML335 had minimal impact on the RuR response relative to K_{2P}2.1 I110D (IC_{50} = 0.173 ± 0.021 μM) (Figure 2D; Table 1). Together, these data demonstrate that RuR inhibition is essentially independent of C-type gate activation (Figures 2C and 2D; Table 1) and are consistent with the observed position of RuR above the selectivity filter.

To see whether there might be structural differences in the interaction of RuR with an activated C-type gate, we determined the structure of the K_{2P}2.1 I110D:RuR:ML335 complex at 2.80 Å resolution (Figures 2E, S3C, and S3D; Table S1). This structure is very similar to the K_{2P}2.1 I110D:RuR complex (Figures S3C–S3E) ($RMSD_{C\alpha}$ = 0.507 Å) and to the previously determined K_{2P}2.1:ML335 complex (Lolicato et al., 2017) ($RMSD_{C\alpha}$ = 0.480 Å) (Table S2). The structure shows that RuR binds to the Keystone inhibitor site using a pose that is very similar to that in the K_{2P}2.1 I110D:RuR complex. Both I110D side chains coordinate multiple Ru centers through direct interactions to RuR (Figures 2F and 2G) like those in the K_{2P}2.1 I110D:RuR complex and there are van der Waals contacts with residues in the CAP and selectivity filter outer mouth. These fundamental similarities in binding to the Keystone inhibitor site are consistent with the similar IC_{50} values measured with or without C-type gate activation (Figures 2C and 2D; Table 1).

Polynuclear Ruthenium Compounds Inhibit K_{2P}s at a Common Site

The dinuclear oxo-bridged ruthenium compound, Ru360 (Figure 3A) (Ying et al., 1991), has many characteristics in common with RuR (cf. Figure 1A). Ru360 is best known as an inhibitor of the MCU (Baughman et al., 2011; Kirichok et al., 2004; Oxenoid et al., 2016), a property it shares with RuR (Gunter and Pfeiffer, 1990). Yet, despite its structural similarity to RuR and the fact that both Ru360 and RuR inhibit MCU, Ru360 has not been reported to block K_{2P} channels. To ask whether Ru360 might inhibit RuR-sensitive K_{2P} channels, we used TEVC to measure the Ru360 responses of K_{2P}2.1 (TREK-1), K_{2P}2.1 I110D, and the natively RuR-sensitive K_{2P}s, K_{2P}10.1 (TREK-2) (Braun et al., 2015) and K_{2P}9.1 (TASK-3) (Czirjak and Enyedi, 2003; Gonzalez et al., 2013; Musset et al., 2006). Application of 100 μM Ru360 to K_{2P}2.1 (TREK-1) had no effect, consistent with the insensitivity of this channel to RuR (Figures 3B and 3F). However, in stark contrast, Ru360 inhibited all of the RuR-sensitive K_{2P}s with micromolar potency (IC_{50} = 11.3 ± 1.8, 2.8 ± 1.2, and 15.6 ± 2.7 μM for K_{2P}2.1 I110D, K_{2P}10.1 (TREK-2), and K_{2P}9.1 (TASK-3), respectively) (Figures 3C–3F; Table 1). Similar to RuR inhibition, Ru360 block of K_{2P}s was independent of voltage (Figures S4A–S4D). For both K_{2P}2.1 I110D and K_{2P}10.1 (TREK-2) the Ru360 IC_{50} values are >10-fold weaker than those for RuR. Because there is a reported 30-fold discrepancy in the IC_{50} of RuR for K_{2P}9.1 (TASK-3) in the literature (0.35 μM [Czirjak and Enyedi, 2003] versus10 μM [Gonzalez et al., 2013]) that precluded a direct comparison with our Ru360 data, we measured inhibition of K_{2P}9.1 (TASK-3) by RuR to resolve whether RuR and Ru360 had similar or different IC_{50} values for K_{2P}9.1 (TASK-3). Our TEVC experiments measured a sub-micromolar IC_{50} for RuR inhibition of K_{2P}9.1 (TASK-3) (IC_{50} = 0.114 ± 0.021 μM) (Figures S4E and S4F; Table 1) that agrees with other *Xenopus* oocyte TEVC studies (Czirjak and Enyedi, 2003). These data establish that, as with the other polynuclear ruthenium-sensitive K_{2P}s we studied, Ru360 is a weaker inhibitor of K_{2P}9.1 (TASK-3) than RuR. The uniformly weaker potency of Ru360 versus RuR against K_{2P}s correlates with the fact that Ru360 carries half the positive charge of RuR (+3 versus +6) and underscores the important role that electrostatics plays in the binding of these polycations.

To understand the details of how Ru360 inhibits K_{2P}s, we determined a 3.51-Å resolution X-ray crystal structure of the K_{2P}2.1 I110D:Ru360 complex (Figures 3G, 3H, S4G, and S4H; Table S1). As with the RuR complexes, the K_{2P}2.1 I110D:Ru360 complex has a channel structure that is overall very similar to the structure of K_{2P}2.1 I110D in the absence of the inhibitor ($RMSD_{C\alpha}$ = 0.665 Å) and to the K_{2P}2.1 I110D:RuR complex ($RMSD_{C\alpha}$ = 0.561 Å) (Figure S4G; Table S2). Ru360 binds to the Keystone inhibitor site in a pose that matches RuR (Figures 3H

Figure 3. Functional and Structural Analysis of K_{2P}:Ru360: Interactions

(A) Ru360 structure.

(B–E) Exemplar TEVC recordings of (B) K_{2P}2.1 (TREK-1), (C) K_{2P}2.1 I110D, (D) K_{2P}10.1 (TREK-2), and (E) K_{2P}9.1 (TASK-3) alone (black) and in the presence of 90 μM Ru360 (green, teal, and olive, respectively).

(F) Ru360 dose-response curves for K_{2P}2.1 I110D (green), K_{2P}2.1 (TREK-1) (light green), K_{2P}10.1 (TREK-2) (teal), and K_{2P}9.1 (TASK-3) (olive). Dashed line shows RuR dose-response for K_{2P}2.1 I110D from Figure 1D. Error bars are SEM.

(G) Structure of the K_{2P}2.1 I110D:Ru360 complex. Inset shows the location of the Ru360 binding site. I110D is shown as sticks.

(H) Close-up view of K_{2P}2.1 I110D (cyan), K_{2P}2.1 I110D:RuR (pink), and K_{2P}2.1 I110D:Ru360 Keystone inhibitor sites. RuR and Ru360 are shown as sticks. S0 ion from the K_{2P}2.1 I110D structure is shown as a sphere.

(I) LigPLOT (Wallace et al., 1995) diagram of K_{2P}2.1 I110D:Ru360 interactions showing ionic interactions (dashed lines) and van der Waals contacts (red) ≤5 Å. Subscripts indicate chain A and chain B residues.

See also Figure S4 and Tables S1 and S2.

and S4G–S4I). Notably, even though Ru360 has one fewer ruthenium atoms than RuR, one of the Ru360 ruthenium amine moieties, denoted Ru_A, occupies essentially the same site as the RuR Ru_A moiety and overlaps with the S0 ion site (Figure 3H), while the other ruthenium amine, Ru_B, overlaps the position of the RuR Ru_B moiety and blocks one EIP arm. There are essentially no conformational changes between K_{2P}2.1 I110D and the K_{2P}2.1 I110D:Ru360 complex except for a change near the base of the CAP helices similar to that seen in the RuR complexes (Figure S4I). The Keystone inhibitor site acidic side chains directly coordinate the Ru360 Ru_A and Ru_B centers (Figure 3I). Ru360 also makes van der Waals contacts to the upper part of the selectivity filter and part of the CAP from chain A similar to those made by RuR (cf. Figures 1H, 2G, and 3I). Together, these data demonstrate that Ru360 inhibits RuR-sensitive K_{2P}s and reveals the common mode by which polynuclear ruthenium amines affect K_{2P} channels by binding to the Keystone inhibitor site, blocking ion exit from the selectivity filter, and obstructing one EIP arm.

Protein Engineering Creates RuR Super-Responders

Because the electronegative nature of the Keystone inhibitor site is a key determinant of K_{2P} channel sensitivity to polynuclear ruthenium compounds, we wanted to test whether increasing the electronegative character of surrounding portions of the EIP would also affect RuR block. To identify candidate sites, we looked for elements on the floor of the RuR and Ru360 binding site that made close contacts with the inhibitors. This analysis identified the backbone atoms of the selectivity filter outer mouth residues Asn147 and Asp256 as the nearest neighbors (Figures 4A and 4B). As we cannot easily change the backbone atoms, we considered changing the properties of the side chains from these positions. Sequence comparison of representatives from each K_{2P} subtype (Figure S5A) shows that the two sites have very different conservation patterns. The Asn147 site shows a range of amino acid types. This variability contrasts with the strict conservation at the Asp256 site. Because all K_{2P}s have aspartate at the 256 position regardless of whether or not they are RuR sensitive, we reasoned that the negatively charged side chain at this site has no influence on RuR binding. By contrast, the amino acid diversity at the Asn147 site indicated that this site might have different properties than the Asp256 site. Hence, we tested whether replacing Asn147 with a negatively charged residue would impact K_{2P}2.1 (TREK-1) RuR sensitivity. TEVC experiments showed that RuR inhibited both K_{2P}2.1 N147D and K_{2P}2.1 N147E (Figures 4C–4F), demonstrating that the presence of an acidic residue at the top of the Keystone inhibitor site is not the only means by which a K_{2P} channel can acquire RuR sensitivity. Notably, there was a marked difference in the IC_{50} values between the two mutants with N147E having a much greater susceptibility to RuR inhibition than N147D (IC_{50} = 0.0733 ± 0.0165 and 47.7 ± 6.3 μM for K_{2P}2.1 N147E and K_{2P}2.1 N147D, respectively) (Figure 4F; Table 1). Similar to RuR inhibition of other K_{2P}s, RuR block of K_{2P}2.1 N147E was essentially voltage independent, whereas K_{2P}2.1 N147D showed a mild voltage dependence (Figures S5B–S5E).

Because both N147D and N147E changes were able to confer RuR sensitivity to K_{2P}2.1 (TREK-1) (Figure 4F; Table 1), we asked whether having negatively charged residues on both the ceiling (residue 110) and floor (residue 147) of the RuR binding site would result in enhanced RuR inhibition. TEVC measurements of the RuR responses of K_{2P}2.1 I110D/N147D and K_{2P}2.1 I110D/N147E revealed that both double mutants had similar IC_{50} values (IC_{50} = 0.0127 ± 0.0023 and 0.0126 ± 0.0034 μM for K_{2P}2.1 I110D/N147D and K_{2P}2.1 I110D/N147E, respectively) (Figures 4G–4I, S5F, and S5G; Table 1). Similar to the I110D and N147E mutants, the response of both double mutant channels to RuR was essentially independent of voltage (Figures S5H–S5J).

The IC_{50} values of the double mutants were an order of magnitude better than that of K_{2P}2.1 I110D alone and three orders of magnitude better than K_{2P}2.1 N147D. Hence, we turned to double mutant cycle analysis (Carter et al., 1984; Hidalgo and MacKinnon, 1995) to assess the extent of synergy between the two sites with respect to RuR inhibition. This analysis uncovered a strong positive cooperativity for the I110D/N147D pair with respect to RuR binding ($\Delta\Delta G = -4.1$ kcal mol^{-1}) (Figure S6A). By contrast, the enhanced RuR response of the I110D/N147E combination resulted from essentially additive contributions of the two negatively charged residues ($\Delta\Delta G = -0.3$ kcal mol^{-1}) (Figure S6B). The fact that the two double mutant pairs do not behave equivalently even though both comprise two sets of acidic side chains, together with the observation that there is a substantial difference in the impact of I110D versus I110E alone on the RuR sensitivity of K_{2P}2.1 (TREK-1) (Figure 1D; Table 1), reinforces the idea that RuR molecular recognition requires both general electrostatic interactions and the direct coordination from the acidic side chains. Taken together, our results suggest that details of these two factors tune the strength of the RuR interaction with the channel. Because of the largely conserved nature of the K_{2P} architecture in the region of the CAP and selectivity filter (Brohawn et al., 2012; Dong et al., 2015; Lolicato et al., 2017; Miller and Long, 2012), installing acidic residues simultaneously at the equivalents of the K_{2P}2.1 (TREK-1) Ile110 and Asn147 positions should endow any K_{2P} of interest sensitive to nanomolar concentrations of RuR.

DISCUSSION

Polynuclear ruthenium compounds have been used for nearly 50 years to control the function of various ion channels (Arif Pavel et al., 2016; Braun et al., 2015; Caterina et al., 1997, 1999; Chaudhuri et al., 2013; Coste et al., 2012; Czirjak and Enyedi, 2003; Dreses-Werringloer et al., 2013; Gonzalez et al., 2013; Guler et al., 2002; Kirichok et al., 2004; Ma, 1993; Ma et al., 2012; Moore, 1971; Musset et al., 2006; Rahamimoff and Alnaes, 1973; Smith et al., 1988; Story et al., 2003; Strotmann et al., 2000; Voets et al., 2002, 2004; Zhao et al., 2016). Yet, despite this widespread application in the study of a multitude of diverse ion channels, there is only limited visualization of how such compounds might interact with and affect the function of their targets (Choi et al., 2019). The K_{2P}:RuR and K_{2P}:Ru360 complexes presented here provide the first detailed structural views of how this class of inorganic polycations can inhibit ion channel function. The structures demonstrate general molecular recognition principles in which a channel uses acidic side chains to coordinate both trinuclear, RuR, and dinuclear, Ru360, ruthenium amines through direct, multipronged electrostatic interactions. Both compounds block the flow of ions through the channel using a

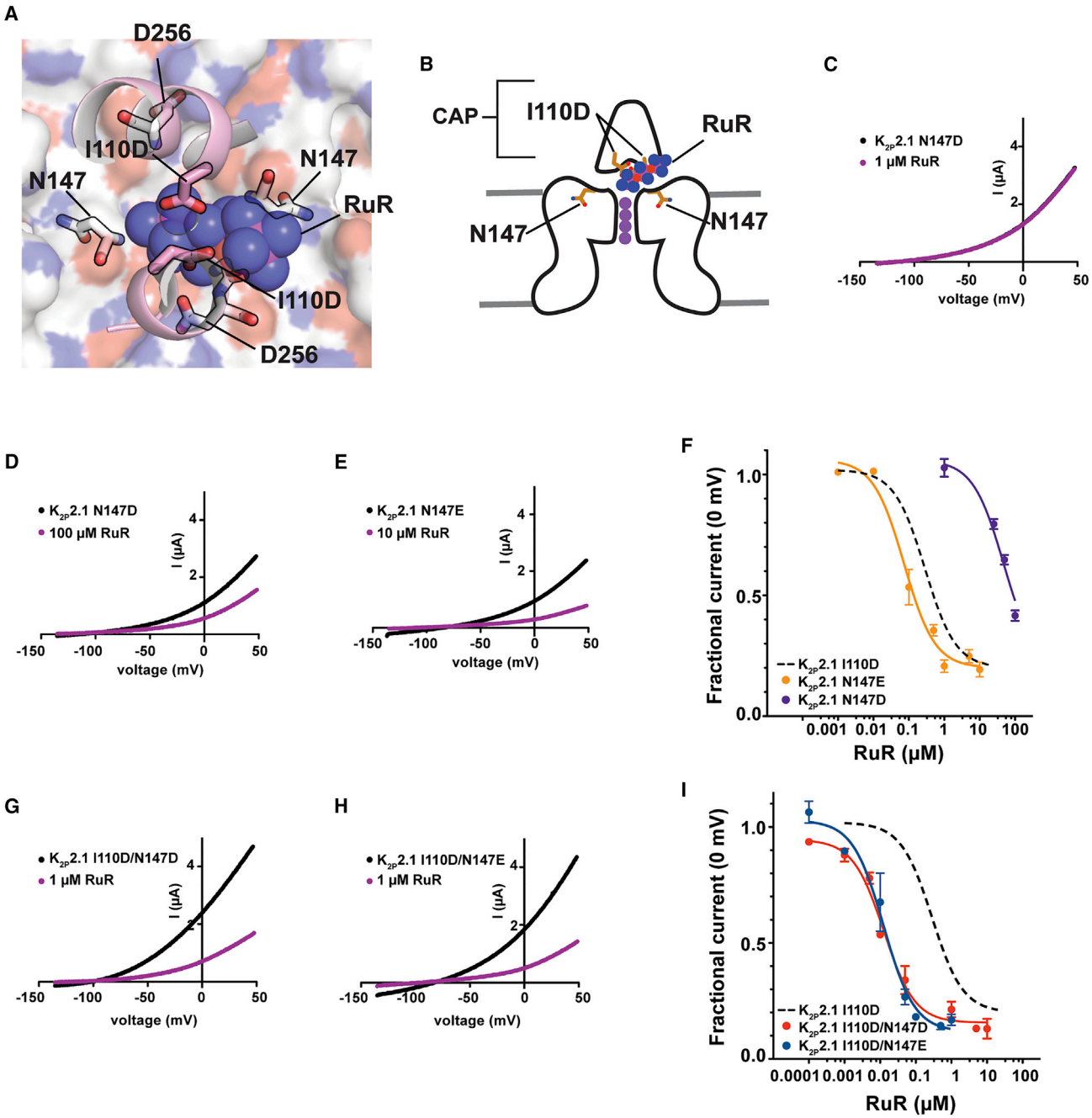

Figure 4. Engineering K_{2P} RuR Super-responders

(A) View through the K_{2P}2.1 I110D CAP to the floor of the Keystone inhibitor site. CAP H2 helix (pink) is shown as a cartoon. RuR is shown as semi-transparent spheres. Surface (white) shows the top of the selectivity filter. I110D, N147, and D256 are shown as sticks.

(B) Cartoon depiction of the elements framing the Keystone inhibitor site. Locations of CAP, I110D, and N147 are indicated. Selectivity filter potassium ions are shown as purple circles.

(C–E) TEVC recordings of (C) K_{2P}2.1 N147D alone (black) and in the presence of 1 μM RuR (magenta), (D) K_{2P}2.1 N147D alone (black) and in the presence of 100 μM RuR (magenta), and (E) K_{2P}2.1 N147E alone (black) and in the presence of 10 μM RuR (magenta).

(F) RuR response of K_{2P}2.1 N147D (purple) and K_{2P}2.1 N147E (orange). Dashed line shows K_{2P}2.1 I110D response to RuR, from Figure 1D. Error bars are SEM.

(G and H) TEVC recordings of (G) K_{2P}2.1 I110D/N147D alone (black) and in the presence of 1 μM RuR (magenta), and (H) K_{2P}2.1 I110D/N147E alone (black) and in the presence of 1 μM RuR (magenta).

(I) RuR dose-response of K_{2P}2.1 I110D/N147D (red) and K_{2P}2.1 I110D/N147E (blue). Dashed line shows K_{2P}2.1 I110D response to RuR, from Figure 1D. Error bars are SEM.

See also Figures S5 and S6.

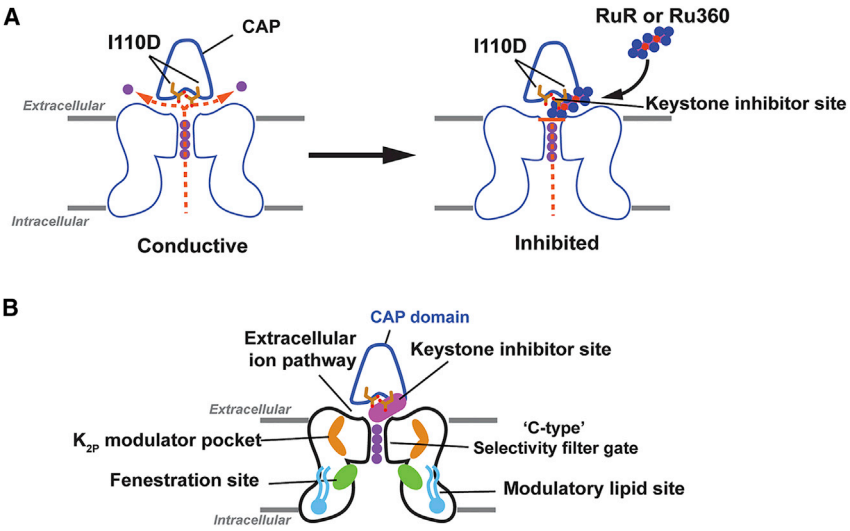

Figure 5. Mechanisms of Small-Molecule K_{2P} Modulation

(A) Cartoon diagram depicting the "finger in the dam" mechanism of K_{2P} inhibition by polynuclear ruthenium amines. Ion flow is indicated by the dashed orange lines. Potassium ions are shown as purple circles.

(B) Polysite model of K_{2P} modulation. Diagram shows structurally defined sites for K_{2P} modulators: Keystone inhibitor site (magenta), K_{2P} modulator pocket (orange) (Lolicato et al., 2017), fenestration site (green) (Dong et al., 2015; Schewe et al., 2019), and modulatory lipid site (cyan) (Lolicato et al., 2017). Extracellular ion pathway and "C-type" selectivity filter gate are indicated. CAP is outlined in blue and shows the position of the negatively charged residues required for the Keystone inhibitor site (sticks).

"finger in the dam" mechanism that exploits the unique archway architecture that the K_{2P} CAP domain creates above the K_{2P} channel mouth in which the terminal end of the polyruthenium compound occupies a site directly over the source of ion flow, the column of ions in the channel selectivity filter (Figure 5A).

K_{2P}s are the only potassium channel family that bears a CAP domain, an extracellular dimerization domain positioned directly above the channel pore (Brohawn et al., 2012; Miller and Long, 2012). The structures presented here show that a pair of aspartic acids located on the underside of the CAP archway at a site that controls the RuR response of natively RuR-sensitive K_{2P}s, K_{2P}10.1 (TREK-2) and K_{2P}9.1 (TASK-3) (Czirjak and Enyedi, 2003; Gonzalez et al., 2013; Musset et al., 2006) and of the RuR-sensitive mutant K_{2P}2.1 I110D (Braun et al., 2015) create a polycation binding site, the Keystone inhibitor site (Figures 1E and 1F). This site forms the primary point of interaction with a single RuR or Ru360 that plugs one arm of the bifurcated EIP created by the CAP domain archway (Figures 1E–1G, 2E, 2F, 3G, and 3H). This structural observation defines an unambiguous mechanism of action for how polyruthenium amines inhibit K_{2P}s, as holding a large polycation above the channel pore would both physically block ion exit as well as provide an electrostatic barrier to permeant ion movement (Figure 5A). Ru360 a dinuclear oxo-bridged ruthenium amine inhibitor of the MCU (Baughman et al., 2011; Kirichok et al., 2004; Oxenoid et al., 2016) that had not previously been reported to affect potassium channels also inhibits engineered, K_{2P}2.1 I110D, and natively RuR-sensitive K_{2P}s, K_{2P}10.1 (TREK-2), and K_{2P}9.1 (TASK-3), in a manner similar to RuR (Figures 3C–3F). Hence, even though RuR and Ru360 bind to a largely pre-formed binding site, there is sufficient plasticity to permit the binding of different types of polyruthenium cations. Consistent with a binding site positioned above the selectivity filter and outside of the transmembrane electric field, polynuclear ruthenium amine inhibition of K_{2P}s is independent of voltage (Figures S1D–S1G, S4A–S4D, S5B–S5E, and S5H–S5J) and C-type gate activation (Figures 2C and 2D). Together, the data define a mechanism of action in which polynuclear ruthenium amines inhibit K_{2P} function by preventing ion flow out of the K_{2P} selectivity filter and through the EIP (Figure 5A).

Although many ion channels lack the extracellular archway made by the K_{2P} CAP domain, the structures of the K_{2P}:polyruthenium amine complexes reveal general molecular recognition principles that are likely to be shared with RuR and Ru360-sensitive ion channels. The requirement to have a negatively charged residue at the Keystone inhibitor site for RuR (Figure 1D) (Braun et al., 2015; Czirjak and Enyedi, 2003; Gonzalez et al., 2013; Musset et al., 2006) and Ru360 (Figure 3F) responses, together with the observation that inhibitor potency is proportional to the total charge (Table 1) highlights the importance of electrostatic interactions for recognizing ruthenium polycations. The multipronged direct coordination of the RuR and Ru360 ruthenium amine moieties (Figures 1H, 2G, and 3I) shows the important role that direct coordination by acidic side chains plays in binding both compounds. The observation that equivalently charged residues having different side chain geometries, aspartate and glutamate, have differential effects on RuR potency at the Keystone inhibitor site (Figure 1D; Table 1) highlights the importance of direct ligand coordination for tuning the strength of the interaction with polynuclear ruthenium amines. It should be noted that K_{2P}4.1 (TRAAK) is inhibited by RuR but lacks a negatively charged residue in the Keystone inhibitor site (Figure S1A) and binds RuR with a higher stoichiometry than observed for the K_{2P} channels studied here (Table 1) (Braun et al., 2015; Czirjak and Enyedi, 2002). These differences suggest that RuR inhibition of K_{2P}4.1 (TRAAK) occurs using a mechanism different from the "finger in the dam" mechanism. Given the importance of direct interactions between RuR and Ru360 and the acidic side chains in the target channels studied here and the fact that acidic residues are key to the RuR sensitivity of other channels (Zhao et al., 2016, 2018), we expect that similar types of multipronged coordination by side chain carboxylates are likely to contribute to the RuR and Ru360 block of other polynuclear ruthenium amine-sensitive channels, such as K_{2P}4.1 (TRAAK), TRPs (Arif Pavel et al., 2016; Caterina et al., 1997, 1999; Guler et al., 2002; Story et al., 2003; Strotmann et al., 2000; Voets et al., 2002, 2004), the MCU (Chaudhuri et al.,

2013; Kirichok et al., 2004; Moore, 1971; Rahamimoff and Alnaes, 1973), CALHM calcium channels (Choi et al., 2019; Dreses-Werringloer et al., 2013; Ma et al., 2012), ryanodine receptors (Ma, 1993; Smith et al., 1988), and Piezo channels (Coste et al., 2012; Zhao et al., 2016), even if the details of where the inhibitor binds to the channel differ.

K_{2P} channels can be modulated by a number of different small molecules and lipids (Sterbuleac, 2019). When placed in the context of previous structural studies of K_{2P} modulator interactions (Dong et al., 2015; Lolicato et al., 2017; Schewe et al., 2019), our studies highlight an emerging picture of the complex, multisite structural pharmacology that contributes to the control of K_{2P} function. The discovery of the Keystone inhibitor site reveals that there are at least four control sites that span from the inner leaflet of the bilayer to the extracellular parts of the channel through which exogenous molecules affect channel function (Figure 5B). These include a modulatory lipid binding site in the bilayer inner leaflet (Lolicato et al., 2017), the fenestration site residing at the intersection of the movable M4 transmembrane helix and the lower part of the selectivity filter that can be targeted by both small-molecule activators and inhibitors (Dong et al., 2015; Schewe et al., 2019), the K_{2P} modulator pocket site (Lolicato et al., 2017), and the Keystone inhibitor site. Exploring the degree of conformational coupling among these modulatory sites will be important for understanding the extent of synergistic or antagonistic actions within the various classes of K_{2P} modulators. Acquiring this type of knowledge will be crucial for creating new interventions that could offer exquisite control of K_{2P} function.

The "finger in the dam" inhibitory mechanism defined here provides a blueprint for the development of small-molecule or protein-based K_{2P} modulators that could reach through the EIP to the Keystone inhibitor site. In this regard, exploiting the renewed interest in synthesizing novel polyruthenium amine derivatives (Woods and Wilson, 2019) or designing compounds having moieties that interact with the Keystone inhibitor site but that also make contacts to non-conserved features of CAP exterior could yield subtype-selective modulators. Biologics, such as nanobodies, may be particularly suited to this type of molecular recognition mode. Furthermore, given the highly conserved nature of the K_{2P} channel architecture in the region of the CAP and selectivity filter (Brohawn et al., 2012; Dong et al., 2015; Lolicato et al., 2017; Miller and Long, 2012), the strategies we used to develop RuR super-responders should be applicable to other K_{2P} subfamily members to create subtypes endowed with RuR sensitivity. Because of the observed non-additivity with respect to RuR binding (Figure S6A), introduction of acidic residues at the Asn147 site to make super-responders seems likely to act through direct interactions with the inhibitor; however, complete understanding of how the enhanced affinity arises will require further structural studies. Regardless of the mechanism, such RuR-sensitive channels could be used to dissect the roles of various K_{2P}s in their native physiological settings.

SIGNIFICANCE

Ruthenium Red (RuR) is a trinuclear, oxo-bridged ruthenium amine polycation that has many biological applications, including a ~50-year legacy as an inhibitor of diverse classes of ion channels. RuR inhibits select members of the K_{2P} (KCNK) family, numerous TRP channels, the mitochondrial calcium uniporter, CALHM calcium channels, ryanodine receptors, and Piezo channels. Despite this remarkably wide range of ion channel targets, there are extremely limited structural data describing how RuR binds to any ion channel target. Our studies show how two polyruthenium compounds, RuR and Ru360, inhibit K_{2P} channels through a "finger in the dam" mechanism in which these polycations bind at a novel site, the "Keystone inhibitor site," formed by acidic residue pair under the K_{2P} CAP domain archway above the channel pore. This series of structures, together with functional studies, outlines the molecular recognition principles that govern how RuR and Ru360 bind to specific sites of proteins using a mixture of electrostatics and polyvalent coordination by acidic side chains. These principles are likely to control RuR and Ru360 binding to a wide range of diverse ion channel targets. Moreover, we show that we can use knowledge of these factors to engineer RuR "super-responder" K_{2P}s that have RuR sensitivity in the low nanomolar range. The protein engineering strategy we define should be generally applicable to any K_{2P} of interest and provide a new method for dissecting the function of specific K_{2P}s in complex settings, such as neurons, the brain, and the cardiovascular system. Together, the data define a "finger in the dam" inhibition mechanism acting at a novel K_{2P} inhibitor binding site. These findings highlight the polysite nature of K_{2P} pharmacology and provide a new framework for K_{2P} inhibitor development.

STAR★METHODS

Detailed methods are provided in the online version of this paper and include the following:

- KEY RESOURCES TABLE
- LEAD CONTACT AND MATERIALS AVAILABILITY
  - Materials Availability Statement
- EXPERIMENTAL MODEL AND SUBJECT DETAILS
- METHOD DETAILS
  - Molecular Biology
  - Two-Electrode Voltage Clamp (TEVC) Electrophysiology
  - Protein Expression
  - Protein Purification
  - Crystallization, Structure Determination, and Refinement
  - Mutant Cycle Analysis
- QUANTIFICATION AND STATISTICAL ANALYSIS
- DATA AND CODE AVAILABILITY

SUPPLEMENTAL INFORMATION

Supplemental Information can be found online at https://doi.org/10.1016/j.chembiol.2020.01.011.

ACKNOWLEDGMENTS

We thank V. Nguyen for help in the initial stages of this project, Z. Wong for technical assistance, A. Natale for help with structure comparisons, J. Du

Bois and M. Grabe for helpful discussions, and Y. Kirichok and members of the Minor lab for comments on the manuscript. This work was supported by grant NIH-R01-MH093603 to D.L.M.

AUTHOR CONTRIBUTIONS

L.P. and D.L.M. conceived the study and designed the experiments. L.P. performed molecular biology experiments, two-electrode voltage-clamp recordings, expressed, purified, and crystallized the proteins, and collected diffraction data. L.P. and M.L. determined the structures. L.P. and M.L. analyzed the data. D.L.M. analyzed data and provided guidance and support. L.P., M.L., and D.L.M. wrote the paper.

DECLARATION OF INTERESTS

The other authors declare no competing interests.

Received: December 2, 2019
Revised: January 16, 2020
Accepted: January 27, 2020
Published: February 13, 2020

REFERENCES

Abraham, D.M., Lee, T.E., Watson, L.J., Mao, L., Chandok, G., Wang, H.G., Frangakis, S., Pitt, G.S., Shah, S.H., Wolf, M.J., et al. (2018). The two-pore domain potassium channel TREK-1 mediates cardiac fibrosis and diastolic dysfunction. J. Clin. Invest. *128*, 4843–4855.

Adams, P.D., Afonine, P.V., Bunkoczi, G., Chen, V.B., Davis, I.W., Echols, N., Headd, J.J., Hung, L.W., Kapral, G.J., Grosse-Kunstleve, R.W., et al. (2010). PHENIX: a comprehensive Python-based system for macromolecular structure solution. Acta Crystallogr. D Biol. Crystallogr. *66*, 213–221.

Alloui, A., Zimmermann, K., Mamet, J., Duprat, F., Noel, J., Chemin, J., Guy, N., Blondeau, N., Voilley, N., Rubat-Coudert, C., et al. (2006). TREK-1, a K^+ channel involved in polymodal pain perception. EMBO J. *25*, 2368–2376.

Arif Pavel, M., Lv, C., Ng, C., Yang, L., Kashyap, P., Lam, C., Valentino, V., Fung, H.Y., Campbell, T., Moller, S.G., et al. (2016). Function and regulation of TRPP2 ion channel revealed by a gain-of-function mutant. Proc. Natl. Acad. Sci. U S A *113*, E2363–E2372.

Bagriantsev, S.N., Peyronnet, R., Clark, K.A., Honore, E., and Minor, D.L., Jr. (2011). Multiple modalities converge on a common gate to control K2P channel function. EMBO J. *30*, 3594–3606.

Bagriantsev, S.N., Clark, K.A., and Minor, D.L., Jr. (2012). Metabolic and thermal stimuli control K(2P)2.1 (TREK-1) through modular sensory and gating domains. EMBO J. *31*, 3297–3308.

Bagriantsev, S.N., Ang, K.H., Gallardo-Godoy, A., Clark, K.A., Arkin, M.R., Renslo, A.R., and Minor, D.L., Jr. (2013). A high-throughput functional screen identifies small molecule regulators of temperature- and mechano-sensitive K2P channels. ACS Chem. Biol. *8*, 1841–1851.

Baughman, J.M., Perocchi, F., Girgis, H.S., Plovanich, M., Belcher-Timme, C.A., Sancak, Y., Bao, X.R., Strittmatter, L., Goldberger, O., Bogorad, R.L., et al. (2011). Integrative genomics identifies MCU as an essential component of the mitochondrial calcium uniporter. Nature *476*, 341–345.

Braun, G., Lengyel, M., Enyedi, P., and Czirjak, G. (2015). Differential sensitivity of TREK-1, TREK-2 and TRAAK background potassium channels to the polycationic dye ruthenium red. Br. J. Pharmacol. *172*, 1728–1738.

Brohawn, S.G., del Marmol, J., and MacKinnon, R. (2012). Crystal structure of the human K2P TRAAK, a lipid- and mechano-sensitive K^+ ion channel. Science *335*, 436–441.

Brohawn, S.G., Wang, W., Handler, A., Campbell, E.B., Schwarz, J.R., and MacKinnon, R. (2019). The mechanosensitive ion channel TRAAK is localized to the mammalian node of Ranvier. eLife *8*, https://doi.org/10.7554/eLife.50403.

Carter, P.J., Winter, G., Wilkinson, A.J., and Fersht, A.R. (1984). The use of double mutants to detect structural changes in the active site of the tyrosyl-tRNA synthetase (*Bacillus stearothermophilus*). Cell *38*, 835–840.

Caterina, M.J., Schumacher, M.A., Tominaga, M., Rosen, T.A., Levine, J.D., and Julius, D. (1997). The capsaicin receptor: a heat-activated ion channel in the pain pathway. Nature *389*, 816–824.

Caterina, M.J., Rosen, T.A., Tominaga, M., Brake, A.J., and Julius, D. (1999). A capsaicin-receptor homologue with a high threshold for noxious heat. Nature *398*, 436–441.

Chaudhuri, D., Sancak, Y., Mootha, V.K., and Clapham, D.E. (2013). MCU encodes the pore conducting mitochondrial calcium currents. eLife *2*, e00704.

Choi, W., Clemente, N., Sun, W., Du, J., and Lu, W. (2019). The structures and gating mechanism of human calcium homeostasis modulator 2. Nature *576*, 163–167.

Clarke, M.J. (2002). Ruthenium metallopharmaceuticals. Coord. Chem. Rev. *232*, 69–93.

Coste, B., Xiao, B., Santos, J.S., Syeda, R., Grandl, J., Spencer, K.S., Kim, S.E., Schmidt, M., Mathur, J., Dubin, A.E., et al. (2012). Piezo proteins are pore-forming subunits of mechanically activated channels. Nature *483*, 176–181.

Czirjak, G., and Enyedi, P. (2002). Formation of functional heterodimers between the TASK-1 and TASK-3 two-pore domain potassium channel subunits. J. Biol. Chem. *277*, 5426–5432.

Czirjak, G., and Enyedi, P. (2003). Ruthenium red inhibits TASK-3 potassium channel by interconnecting glutamate 70 of the two subunits. Mol. Pharmacol. *63*, 646–652.

Decher, N., Ortiz-Bonnin, B., Friedrich, C., Schewe, M., Kiper, A.K., Rinne, S., Seemann, G., Peyronnet, R., Zumhagen, S., Bustos, D., et al. (2017). Sodium permeable and "hypersensitive" TREK-1 channels cause ventricular tachycardia. EMBO Mol. Med. *9*, 403–414.

Devilliers, M., Busserolles, J., Lolignier, S., Deval, E., Pereira, V., Alloui, A., Christin, M., Mazet, B., Delmas, P., Noel, J., et al. (2013). Activation of TREK-1 by morphine results in analgesia without adverse side effects. Nat. Commun. *4*, 2941.

Diederichs, K., and Karplus, P.A. (2013). Better models by discarding data? Acta Crystallogr. D Biol. Crystallogr. *69*, 1215–1222.

Dong, Y.Y., Pike, A.C., Mackenzie, A., McClenaghan, C., Aryal, P., Dong, L., Quigley, A., Grieben, M., Goubin, S., Mukhopadhyay, S., et al. (2015). K2P channel gating mechanisms revealed by structures of TREK-2 and a complex with Prozac. Science *347*, 1256–1259.

Douguet, D., and Honore, E. (2019). Mammalian mechanoelectrical transduction: structure and function of force-gated ion channels. Cell *179*, 340–354.

Dreses-Werringloer, U., Vingtdeux, V., Zhao, H., Chandakkar, P., Davies, P., and Marambaud, P. (2013). CALHM1 controls the Ca(2)(+)-dependent MEK, ERK, RSK and MSK signaling cascade in neurons. J. Cell Sci. *126*, 1199–1206.

Emsley, P., and Cowtan, K. (2004). Coot: model-building tools for molecular graphics. Acta Crystallogr. D Biol. Crystallogr. *60*, 2126–2132.

Enyedi, P., and Czirjak, G. (2010). Molecular background of leak K^+ currents: two-pore domain potassium channels. Physiol. Rev. *90*, 559–605.

Evans, P.R., and Murshudov, G.N. (2013). How good are my data and what is the resolution? Acta Crystallogr. D Biol. Crystallogr. *69*, 1204–1214.

Feliciangeli, S., Chatelain, F.C., Bichet, D., and Lesage, F. (2014). The family of K channels: salient structural and functional properties. J Physiol. https://doi.org/10.1113/jphysiol.2014.287268.

Fletcher, J.M., Greenfield, B.F., Hardy, C.J., Scargill, D., and Woodhead, J.L. (1961). Ruthenium red. J. Chem. Soc. 2000–2006.

Gonzalez, W., Zuniga, L., Cid, L.P., Arevalo, B., Niemeyer, M.I., and Sepulveda, F.V. (2013). An extracellular ion pathway plays a central role in the cooperative gating of a K(2P) K^+ channel by extracellular pH. J. Biol. Chem. *288*, 5984–5991.

Guler, A.D., Lee, H., Iida, T., Shimizu, I., Tominaga, M., and Caterina, M. (2002). Heat-evoked activation of the ion channel, TRPV4. J. Neurosci. *22*, 6408–6414.

Gunter, T.E., and Pfeiffer, D.R. (1990). Mechanisms by which mitochondria transport calcium. Am. J. Physiol. *258*, C755–C786.

Heurteaux, C., Guy, N., Laigle, C., Blondeau, N., Duprat, F., Mazzuca, M., Lang-Lazdunski, L., Widmann, C., Zanzouri, M., Romey, G., et al. (2004). TREK-1, a K^+ channel involved in neuroprotection and general anesthesia. EMBO J. *23*, 2684–2695.

Heurteaux, C., Lucas, G., Guy, N., El Yacoubi, M., Thummler, S., Peng, X.D., Noble, F., Blondeau, N., Widmann, C., Borsotto, M., et al. (2006). Deletion of the background potassium channel TREK-1 results in a depression-resistant phenotype. Nat. Neurosci. *9*, 1134–1141.

Hidalgo, P., and MacKinnon, R. (1995). Revealing the architecture of a K^+ channel pore through mutant cycles with a peptide inhibitor. Science *268*, 307–310.

Kabsch, W. (2010). Xds. Acta Crystallogr. D Biol. Crystallogr. *66*, 125–132.

Kanda, H., Ling, J., Tonomura, S., Noguchi, K., Matalon, S., and Gu, J.G. (2019). TREK-1 and TRAAK are principal K(+) channels at the nodes of Ranvier for rapid action potential conduction on mammalian myelinated afferent nerves. Neuron *104*, 960–971.e7.

Kawate, T., and Gouaux, E. (2006). Fluorescence-detection size-exclusion chromatography for precrystallization screening of integral membrane proteins. Structure *14*, 673–681.

Kirichok, Y., Krapivinsky, G., and Clapham, D.E. (2004). The mitochondrial calcium uniporter is a highly selective ion channel. Nature *427*, 360–364.

Laigle, C., Confort-Gouny, S., Le Fur, Y., Cozzone, P.J., and Viola, A. (2012). Deletion of TRAAK potassium channel affects brain metabolism and protects against ischemia. PLoS One *7*, e53266.

Lambert, M., Boet, A., Rucker-Martin, C., Mendes-Ferreira, P., Capuano, V., Hatem, S., Adao, R., Bras-Silva, C., Hautefort, A., Michel, J.B., et al. (2018). Loss of KCNK3 is a hallmark of RV hypertrophy/dysfunction associated with pulmonary hypertension. Cardiovasc. Res. *114*, 880–893.

Lazarenko, R.M., Fortuna, M.G., Shi, Y., Mulkey, D.K., Takakura, A.C., Moreira, T.S., Guyenet, P.G., and Bayliss, D.A. (2010). Anesthetic activation of central respiratory chemoreceptor neurons involves inhibition of a THIK-1-like background K(+) current. J. Neurosci. *30*, 9324–9334.

Lolicato, M., Riegelhaupt, P.M., Arrigoni, C., Clark, K.A., and Minor, D.L., Jr. (2014). Transmembrane helix straightening and buckling underlies activation of mechanosensitive and thermosensitive K(2P) channels. Neuron *84*, 1198–1212.

Lolicato, M., Arrigoni, C., Mori, T., Sekioka, Y., Bryant, C., Clark, K.A., and Minor, D.L., Jr. (2017). K2P2.1 (TREK-1)-activator complexes reveal a cryptic selectivity filter binding site. Nature *547*, 364–368.

Ma, J. (1993). Block by ruthenium red of the ryanodine-activated calcium release channel of skeletal muscle. J. Gen. Physiol. *102*, 1031–1056.

Ma, Z., Siebert, A.P., Cheung, K.H., Lee, R.J., Johnson, B., Cohen, A.S., Vingtdeux, V., Marambaud, P., and Foskett, J.K. (2012). Calcium homeostasis modulator 1 (CALHM1) is the pore-forming subunit of an ion channel that mediates extracellular Ca^{2+} regulation of neuronal excitability. Proc. Natl. Acad. Sci. U S A *109*, E1963–E1971.

Madry, C., Kyrargyri, V., Arancibia-Carcamo, I.L., Jolivet, R., Kohsaka, S., Bryan, R.M., and Attwell, D. (2018). Microglial ramification, surveillance, and interleukin-1beta release are regulated by the two-pore domain K(+) channel THIK-1. Neuron *97*, 299–312.e6.

Miller, A.N., and Long, S.B. (2012). Crystal structure of the human two-pore domain potassium channel K2P1. Science *335*, 432–436.

Moore, C.L. (1971). Specific inhibition of mitochondrial Ca^{++} transport by ruthenium red. Biochem. Biophys. Res. Commun. *42*, 298–305.

Murshudov, G.N., Vagin, A.A., and Dodson, E.J. (1997). Refinement of macromolecular structures by the maximum-likelihood method. Acta Crystallogr. D Biol. Crystallogr. *53*, 240–255.

Musset, B., Meuth, S.G., Liu, G.X., Derst, C., Wegner, S., Pape, H.C., Budde, T., Preisig-Muller, R., and Daut, J. (2006). Effects of divalent cations and spermine on the K^+ channel TASK-3 and on the outward current in thalamic neurons. J. Physiol. *572*, 639–657.

Oxenoid, K., Dong, Y., Cao, C., Cui, T., Sancak, Y., Markhard, A.L., Grabarek, Z., Kong, L., Liu, Z., Ouyang, B., et al. (2016). Architecture of the mitochondrial calcium uniporter. Nature *533*, 269–273.

Piechotta, P.L., Rapedius, M., Stansfeld, P.J., Bollepalli, M.K., Ehrlich, G., Andres-Enguix, I., Fritzenschaft, H., Decher, N., Sansom, M.S., Tucker, S.J., et al. (2011). The pore structure and gating mechanism of K2P channels. EMBO J. *30*, 3607–3619.

Pope, L., Arrigoni, C., Lou, H., Bryant, C., Gallardo-Godoy, A., Renslo, A.R., and Minor, D.L., Jr. (2018). Protein and chemical determinants of BL-1249 action and selectivity for K2P channels. ACS Chem. Neurosci. *9*, 3153–3165.

Rahamimoff, R., and Alnaes, E. (1973). Inhibitory action of ruthenium red on neuromuscular transmission. Proc. Natl. Acad. Sci. U S A *70*, 3613–3616.

Renigunta, V., Schlichthorl, G., and Daut, J. (2015). Much more than a leak: structure and function of K(2)p-channels. Pflugers Arch. *467*, 867–894.

Rödström, K.E.J., Kiper, A.K., Zhang, W., Rinné, S., Pike, A.C.W., Goldstein, M., Conrad, L., Delbeck, M., Hahn, M., Meier, H., et al. (2019). A unique lower X-gate in TASK channels traps inhibitors within the vestibule. bioRxiv, 706168, https://doi.org/10.1101/706168.

Royal, P., Andres-Bilbe, A., Avalos Prado, P., Verkest, C., Wdziekonski, B., Schaub, S., Baron, A., Lesage, F., Gasull, X., Levitz, J., et al. (2019). Migraine-associated TRESK mutations increase neuronal excitability through alternative translation initiation and inhibition of TREK. Neuron *101*, 232–245.e6.

Schewe, M., Nematian-Ardestani, E., Sun, H., Musinszki, M., Cordeiro, S., Bucci, G., de Groot, B.L., Tucker, S.J., Rapedius, M., and Baukrowitz, T. (2016). A non-canonical voltage-sensing mechanism controls gating in K2P K(+) channels. Cell *164*, 937–949.

Schewe, M., Sun, H., Mert, U., Mackenzie, A., Pike, A.C.W., Schulz, F., Constantin, C., Vowinkel, K.S., Conrad, L.J., Kiper, A.K., et al. (2019). A pharmacological master key mechanism that unlocks the selectivity filter gate in K(+) channels. Science *363*, 875–880.

Shaya, D., Kreir, M., Robbins, R.A., Wong, S., Hammon, J., Bruggemann, A., and Minor, D.L., Jr. (2011). Voltage-gated sodium channel (NaV) protein dissection creates a set of functional pore-only proteins. Proc. Natl. Acad. Sci. U S A *108*, 12313–12318.

Smith, J.S., Imagawa, T., Ma, J., Fill, M., Campbell, K.P., and Coronado, R. (1988). Purified ryanodine receptor from rabbit skeletal muscle is the calcium-release channel of sarcoplasmic reticulum. J. Gen. Physiol. *92*, 1–26.

Sterbuleac, D. (2019). Molecular determinants of chemical modulation of two-pore domain potassium channels. Chem. Biol. Drug Des. *94*, 1596–1614.

Story, G.M., Peier, A.M., Reeve, A.J., Eid, S.R., Mosbacher, J., Hricik, T.R., Earley, T.J., Hergarden, A.C., Andersson, D.A., Hwang, S.W., et al. (2003). ANKTM1, a TRP-like channel expressed in nociceptive neurons, is activated by cold temperatures. Cell *112*, 819–829.

Strotmann, R., Harteneck, C., Nunnenmacher, K., Schultz, G., and Plant, T.D. (2000). OTRPC4, a nonselective cation channel that confers sensitivity to extracellular osmolarity. Nat. Cell Biol. *2*, 695–702.

Su, Z.W., Brown, E.C., Wang, W.W., and MacKinnon, R. (2016). Novel cell-free high-throughput screening method for pharmacological tools targeting K^+ channels. Proc. Natl. Acad. Sci. U S A *113*, 5748–5753.

Tian, F., Qiu, Y., Lan, X., Li, M., Yang, H., and Gao, Z. (2019). A small-molecule compound selectively activates K2P channel TASK-3 by acting at two distant clusters of residues. Mol. Pharmacol. *96*, 26–35.

Vivier, D., Soussia, I.B., Rodrigues, N., Lolignier, S., Devilliers, M., Chatelain, F.C., Prival, L., Chapuy, E., Bourdier, G., Bennis, K., et al. (2017). Development of the first two-pore domain potassium channel TREK-1 (TWIK-related K^+ channel 1)-selective agonist possessing in vivo anti-nociceptive activity. J. Med. Chem. *60*, 1076–1088.

Voets, T., Prenen, J., Vriens, J., Watanabe, H., Janssens, A., Wissenbach, U., Bodding, M., Droogmans, G., and Nilius, B. (2002). Molecular determinants of permeation through the cation channel TRPV4. J. Biol. Chem. *277*, 33704–33710.

Voets, T., Nilius, B., Hoefs, S., van der Kemp, A.W., Droogmans, G., Bindels, R.J., and Hoenderop, J.G. (2004). TRPM6 forms the Mg^{2+} influx channel involved in intestinal and renal Mg^{2+} absorption. J. Biol. Chem. *279*, 19–25.

Wallace, A.C., Laskowski, R.A., and Thornton, J.M. (1995). LIGPLOT: a program to generate schematic diagrams of protein-ligand interactions. Protein Eng. *8*, 127–134.

Woods, J.J., and Wilson, J.J. (2019). Inhibitors of the mitochondrial calcium uniporter for the treatment of disease. Curr. Opin. Chem. Biol. *55*, 9–18.

Wright, P.D., McCoull, D., Walsh, Y., Large, J.M., Hadrys, B.W., Gaurilcikaite, E., Byrom, L., Veale, E.L., Jerman, J., and Mathie, A. (2019). Pranlukast is a novel small molecule activator of the two-pore domain potassium channel TREK2. Biochem. Biophys. Res. Commun. *520*, 35–40.

Wu, X., Liu, Y., Chen, X., Sun, Q., Tang, R., Wang, W., Yu, Z., and Xie, M. (2013). Involvement of TREK-1 activity in astrocyte function and neuroprotection under simulated ischemia conditions. J. Mol. Neurosci. *49*, 499–506.

Yarishkin, O., Phuong, T.T.T., Bretz, C.A., Olsen, K.W., Baumann, J.M., Lakk, M., Crandall, A., Heurteaux, C., Hartnett, M.E., and Krizaj, D. (2018). TREK-1 channels regulate pressure sensitivity and calcium signaling in trabecular meshwork cells. J. Gen. Physiol. *150*, 1660–1675.

Ying, W.L., Emerson, J., Clarke, M.J., and Sanadi, D.R. (1991). Inhibition of mitochondrial calcium ion transport by an oxo-bridged dinuclear ruthenium ammine complex. Biochemistry *30*, 4949–4952.

Yoshida, K., Shi, S., Ukai-Tadenuma, M., Fujishima, H., Ohno, R.I., and Ueda, H.R. (2018). Leak potassium channels regulate sleep duration. Proc. Natl. Acad. Sci. U S A *115*, E9459–E9468.

Zhao, Q.C., Wu, K., Geng, J., Chi, S.P., Wang, Y.F., Zhi, P., Zhang, M.M., and Xiao, B.L. (2016). Ion permeation and mechanotransduction mechanisms of mechanosensitive piezo channels. Neuron *89*, 1248–1263.

Zhao, Q., Zhou, H., Chi, S., Wang, Y., Wang, J., Geng, J., Wu, K., Liu, W., Zhang, T., Dong, M.Q., et al. (2018). Structure and mechanogating mechanism of the Piezo1 channel. Nature *554*, 487–492.

STAR★METHODS

KEY RESOURCES TABLE

REAGENT or RESOURCE	SOURCE	IDENTIFIER
Chemicals, Peptides, and Recombinant Proteins		
Collagenase	Worthington Biochemical Corporation	Cat#LS004183
Ruthenium Red	Millipore-Sigma	Cat#R2751
Ru360	Millipore-Sigma, Calbiochem	Cat#557440
ML335	Lolicato et al., 2017	N/A
Yeast Nitrogen Base (YNB)	Invitrogen	Cat#Q30007
Anti-GFP Nanobody	Lolicato et al., 2017	N/A
3C Protease	Shaya et al., 2011	N/A
Octyl glucose neopentyl glycol (OGNG)	Anatrace	Cat#NG31125GM
n-heptyl-β-D-thioglucopyranoside (HTG)	Anatrace	Cat#H30125GM
Cholesterol hemisuccinate (CHS)	Anatrace	Cat#CH21025GM
Phenylmethylsulfonyl fluoride (PMSF)	Millipore-Sigma	Cat#P7626
DNase I	Roche	Cat#1010415900
mMessage Machine T7 transcription kit	ThemoFisher	Cat# AM1344
RNEasy kit	Qiagen	Cat# 74104
Deposited Data		
K_{2P}2.1 (TREK-1) I110D (apo) structure	This paper	PDB: 6V36
K_{2P}2.1 (TREK-1) I110D bound to RuR	This paper	PDB: 6V3I
K_{2P}2.1 (TREK-1) I110D co-bound to RuR and ML335	This paper	PDB: 6V37
K_{2P}2.1 (TREK-1) I110D bound to Ru360	This paper	PDB: 6V3C
K_{2P}4.1 (TRAAK) G124I	Lolicato et al., 2014	PDB: 4RUE
K_{2P}2.1 (TREK-1) (apo)	Lolicato et al., 2017	PDB: 6CQ6
K_{2P}2.1 (TREK-1) bound to ML335	Lolicato et al., 2017	PDB: 6CQ8
K_{2P}10.1 (TREK-2) (apo)	Dong et al., 2015	PDB: 4BW5
Experimental Models: Organisms/Strains		
Xenopus laevis (frogs for oocyte removal)	Nasco	Female, 9+CM
Pichia pastoris (SMD1163H)	Lolicato et al., 2017	N/A
Recombinant DNA		
Murine K_{2P}2.1 (TREK-1) (pGEM)	Bagriantsev et al., 2013	N/A
K_{2P}2.1 (TREK-1) I110D (pGEM)	This paper	N/A
K_{2P}2.1 (TREK-1) I110E (pGEM)	This paper	N/A
K_{2P}2.1 (TREK-1) I110K (pGEM)	This paper	N/A
K_{2P}2.1 (TREK-1) I110D/G137I (pGEM)	This paper	N/A
K_{2P}2.1 (TREK-1) N147D (pGEM)	This paper	N/A
K_{2P}2.1 (TREK-1) N147E (pGEM)	This paper	N/A
K_{2P}2.1 (TREK-1) I110D/N147D (pGEM)	This paper	N/A
K_{2P}2.1 (TREK-1) I110D/N147E (pGEM)	This paper	N/A
Murine K_{2P}10.1 (TREK-2) (pGEM)	Bagriantsev et al., 2013	N/A
Murine K_{2P}9.1 (TASK-3) (pGEM)	Bagriantsev et al., 2013	N/A
K_{2P}2.1 (TREK-1)$_{CRYST}$ (pPicZ)	Lolicato et al., 2017	N/A
K_{2P}2.1 (TREK-1)$_{CRYST}$ I110D (pPicZ)	This paper	N/A
Software and Algorithms		
pClamp, Version 8	Molecular Devices	N/A
Clampfit 8.1	Molecular Devices	N/A

(*Continued on next page*)

Continued

REAGENT or RESOURCE	SOURCE	IDENTIFIER
Graphpad Prism, Version 5	Graphpad Software	https://www.graphpad.com/scientific-software/prism/
XDS	Kabsch, 2010	http://xds.mpimf-heidelberg.mpg.de/
Aimless	Evans and Murshudov, 2013	http://www.ccp4.ac.uk/
PHENIX	Adams et al., 2010	https://www.phenix-online.org/
COOT	Emsley and Cowtan, 2004	http://www2.mrc-lmb.cam.ac.uk/personal/pemsley/coot/
REFMAC	Murshudov et al., 1997	http://www.ccp4.ac.uk/
Other		
CNBr-activated sepharose resin	GE Healthcare	Cat#17-0430-01
Superdex 200 column, 10/300	GE Healthcare	Cat#17-5175-01
Econo-Pac gravity column, 1.5 x 12 cm	Bio-Rad	Cat#7321010
GeneClamp 500B	MDS Analytical Technologies	N/A
Synchrotron radiation at APS GM/CAT Beamline 23-IDB/D	APS, Chicago	N/A

LEAD CONTACT AND MATERIALS AVAILABILITY

Further information and request for resources and reagents should be directed to and will be fulfilled by the lead contact, Daniel L. Minor, Jr. (daniel.minor@ucsf.edu).

Materials Availability Statement

All unique reagents generated in this study are available from the Lead Contact with a completed Materials Transfer Agreement.

EXPERIMENTAL MODEL AND SUBJECT DETAILS

Pichia pastoris strain SMD1163H was used for protein expression.

Xenopus laevis oocytes were harvested from female *X. laevis* according to UCSF IACUC Protocol AN129690.

METHOD DETAILS

Molecular Biology

Murine K_{2P}2.1 (TREK-1) (Gene ID: 16526), K_{2P}10.1 (TREK-2) (Gene ID: 72258), and K_{2P}9.1 (TASK-3) (Gene ID: 223604) were each expressed from in a pGEMHE/pMO vector for two-electrode voltage clamp (TEVC) experiments as described previously (Lolicato et al., 2017; Pope et al., 2018). A previously described version of murine K_{2P}2.1 (TREK-1) in a *Pichia pastoris* pPicZ plasmid, K_{2P}2.1(TREK-1)$_{CRYST}$ (Lolicato et al., 2017), encoding residues 21-322 and bearing the following mutations: K84R, Q85E, T86K, I88L, A89R, Q90A, A92P, N95S, S96D, T97Q, N119A, S300C, E306A, was used for structural studies. Mutants of K_{2P}2.1 (TREK-1) and K_{2P}2.1(TREK-1)$_{CRYST}$ were generated using site-directed mutagenesis (PFU Turbo AD, Agilent) and verified by sequencing of the complete gene.

Two-Electrode Voltage Clamp (TEVC) Electrophysiology

Xenopus laevis oocytes were harvested according to UCSF IACUC Protocol AN129690 and digested using collagenase (Worthington Biochemical Corporation, #LS004183, 0.7-0.8 mg mL^{-1}) in Ca^{2+}-free ND96 (96 mM NaCl, 2 mM KCl, 3.8 mM $MgCl_2$, 5 mM HEPES pH 7.4) immediately post-harvest, as previously reported (Lolicato et al., 2017; Pope et al., 2018). Oocytes were maintained at 18°C in ND96 (96 mM NaCl, 2 mM KCl, 1.8 mM $CaCl_2$, 2 mM $MgCl_2$, 5 mM HEPES pH 7.4) supplemented with antibiotics (100 units mL^{-1} penicillin, 100 μg mL^{-1} streptomycin, 50 μg mL^{-1} gentimycin) and used for experiments within one week of harvest. mRNA for oocyte injection was prepared from plasmid DNA using mMessage Machine T7 Transcription Kit (Thermo Fisher Scientific), purified using RNEasy kit (Qiagen), and stored as stocks and dilutions in RNAse-free water at -80°C.

Defolliculated stage V-VI oocytes were microinjected with 50 nL of 0.1-6 ng mRNA and currents were recorded within 24-48 hours of injection. Oocytes were impaled by two standard microelectrodes (0.3-3.0 MΩ), filled with 3M KCl and subjected to constant perfusion of ND96. Currents were elicited from a -80 mV holding potential using a 500 ms ramp ranging from -140 to +50 mV.

Recording solutions containing Ruthenium red (RuR) (Millipore-Sigma, R2751) and Ru360 (Millipore-Sigma, Calbiochem – 557440) were prepared immediately prior to use. RuR was weighed and dissolved directly into ND96 at 200 μM and then diluted into ND96 for tested experimental concentrations. The pH of the stock solution was checked to ensure no change occurred. Due to its instability in

aqueous solutions, Ru360 solutions were covered with aluminum foil to minimize exposure to light and to avoid degradation. RuR and Ru360 were determined to be stable in recording solutions for duration of typical experiment length by measuring UV absorbance at 536 nm and 363 nm, respectively, before and after length of the recording session. ML335 was synthesized as described previously (Lolicato et al., 2017). ML335 recording solutions were prepared from a DMSO stock stored at -20°C (final DMSO concentration was 0.1%).

Data were recorded using a GeneClamp 500B (MDS Analytical Technologies) amplifier controlled by pClamp software (Molecular Devices), and digitized at 1 kHz using Digidata 1332A (MDS Analytical Technologies). For each recording, control solution (ND96) was perfused over a single oocyte until current was stable before switching to solutions containing the test compounds at various concentrations and again allowed to stabilize before recording final, stabilized trace. Fractional block at the potential of interest was determined as $\frac{I-I_B}{I_0-I_B}$ in which I is the measured current, I_0 is the current in the absence of the test compound, and I_B is the basal current derived from an average of uninjected oocytes (n=14). For dose-response curves, each point is an average of at least three oocytes recorded from at least two independent batches of oocytes. Representative traces and dose response plots were generated in Graphpad Prism Version 5 (GraphPad Software, San Diego California USA, www.graphpad.com). Inhibition IC_{50}s were estimated using an auto-fitted Hill equation with a Hill coefficient = -1.0.

Protein Expression

$K_{2P}2.1_{CRYST}$ I110D was expressed as a fusion protein having in series from the channel C-terminus a 3C protease site, green fluorescent protein (GFP), and His_{10} tag as described previously for $K_{2P}2.1_{cryst}$ (Lolicato et al., 2017). Linearized plasmid DNA (PmeI) was introduced into *Pichia pastoris* strain SMD1163H via electroporation. Strains with highest incorporation were selected for on YPD plates containing 1-2 mg mL^{-1} zeocin. Individual colonies were screened using fluorescence size exclusion chromatography (FSEC) (Kawate and Gouaux, 2006) to identify strain with highest expression level as described previously (Lolicato et al., 2017). The best FSEC candidate as judged by FSEC fluorescence intensity was used to inoculate a starter culture (60-120 mL) in minimal media (1% glycerol, 100 mM potassium phosphate pH 6.0, 0.4 mg L^{-1} biotin, 1X YNB from Invitrogen) supplemented with 1 mg mL^{-1} zeocin and cultured in shaker flask for 2 days at 29°C. The starter culture was then used to inoculate a large scale (6-12L) culture in shaker flasks containing minimal media without zeocin. Cells were grown at 29°C over two days in minimal media containing 1% glycerol. Cells were centrifuged at 3000g (6 min, 20°C) and pellet was resuspended in minimal induction media (100 mM potassium phosphate pH 6.0, 0.4 mg L^{-1} biotin, 1X YNB) containing 0.5% methanol. After 24 hrs, 0.5% methanol was added to each flask. Cells were harvested (6000g, 20 min, 4°C) two days after induction, snap-frozen in liquid nitrogen, and stored at -80°C.

Protein Purification

Purified $K_{2P}2.1_{cryst}$ I110D was obtained from preparations using 100-200g of cell mass cryo-milled (Retsch, MM400) in liquid nitrogen (5 x 3 min, 25 Hz). All purification steps were carried out at 4°C and purification conditions were similar to those previously reported for $K_{2P}2.1_{cryst}$ (Lolicato et al., 2017). Cell powder was solubilized at a ratio of 3 grams of cells per mL of lysis buffer containing 200 mM KCl, 21 mM octyl glucose neopentyl glycol (OGNG, Anatrace), 30 mM *n*-heptyl-β-D-thioglucopyranoside (HTG, Anatrace), 0.1% cholesterol hemisuccinate (CHS, Anatrace), 100 mM Tris-Cl, pH 8.2, 1 mM PMSF and 0.1 mg/mL DNaseI. Following 3 hour membrane solubilization, the sample was centrifuged at 40,000g for 45 min at 4°C. After centrifugation, supernatant was incubated with anti-GFP nanobodies immobilized on CNBr-activated sepharose resin (GE Healthcare, 17-0430-01) at a ratio of 1 mL resin per 10 g of cells and gently rotated on an orbital rocker for 3 hours. Resin was collected in a gravity column (Econo-Pac, 1.5 x 12 cm, BioRad) and washed with 10 CV each, buffers A-C (A-C: 200 mM KCl, 50 mM Tris-Cl pH 8.0, 15 mM HTG; A: 10 mM OGNG, 0.018% CHS; B: 5 mM OGNG, 0.018% CHS; C: 3.85 mM OGNG, 0.0156% CHS), applied in series to reduce the detergent concentration and wash away cell debris (30 CV total). The GFP-affinity tag was cleaved overnight on column using two CV of buffer C supplemented with 350 mM KCl, 1 mM EDTA and 3C protease (Shaya et al., 2011). Cleaved protein was eluted from resin with two CV of size-exclusion buffer (SEC: 200 mM KCl, 20 mM Tris-Cl pH 8.0, 2.1 mM OGNG, 15 mM HTG, 0.012% CHS), concentrated and applied to a Superdex 200 (GE, 10/300) pre-equilibrated with SEC buffer. Peak fractions were evaluated by SDS-PAGE (15% acrylamide) for purity, pooled and concentrated for crystallization.

Crystallization, Structure Determination, and Refinement

Purified $K_{2P}2.1_{cryst}$-I110D was concentrated to 6 mg mL^{-1} before crystallization using hanging-drop vapor diffusion at 4°C using a mixture of 0.2 μL protein to 0.1 μL reservoir solution, over 100 μL reservoir of 20-25% PEG400, 200 mM KCl, 100 mM HEPES pH 8.0 or 7.1 and 1-2 mM $CdCl_2$. Crystals appeared within 1-2 days and grew to full size within 2 weeks. Crystals were cryoprotected in solution containing 200 mM KCl, 0.2% OGNG, 15 mM HTG, 0.02% CHS, 100 mM HEPES pH 8.0 or 7.1 and 1-2 mM $CdCl_2$, with 5% increase in PEG400 up to final concentration of 38% before flash freezing in liquid nitrogen. For compound bound structures, cryoprotected crystals were also soaked in final cryoprotection solution containing 1 mM each RuRed, RuRed+ML335 or Ru360, sourced as described in TEVC methods, for at least 1 hour prior to flash freezing in liquid nitrogen.

Datasets were collected at 100 K using synchrotron radiation at APS GM/CAT beamline 23-IDB/D Chicago, Illinois using a wavelength of 1.0332 Å, processed with XDS (Kabsch, 2010) and scaled and merged with Aimless (Evans and Murshudov, 2013). Highest resolution structures were obtained from crystals that were soaked with the ruthenium compounds. Structure determination of low resolution datasets from complexes obtained by co-crystallization indicated that there was no difference in the RuR position in complexes made by either soaking or co-crystallization. Final resolution cutoff was 3.40 Å, 3.40 Å, 2.80 Å and 3.51 Å for $K_{2P}2.1_{cryst}$ I110D,

$K_{2P}2.1_{cryst}$ I110D:RuR, $K_{2P}2.1_{cryst}$ I110D:RuR:ML335 and $K_{2P}2.1_{cryst}$ I110D:Ru360 structures, respectively, using the $CC_{1/2}$ criterion (Diederichs and Karplus, 2013). $K_{2P}2.1_{cryst}$-I110D was solved by molecular replacement utilizing $K_{2P}4.1$ (G124I) structure (PDB: 4RUE) as search model. For compound bound structures, the $K_{2P}2.1_{cryst}$-I110D model was used as the molecular replacement search model. Electron density maps were improved through several cycles of manual model rebuilding, using COOT (Emsley and Cowtan, 2004), REFMAC (Murshudov et al., 1997), and PHENIX (Adams et al., 2010).

Mutant Cycle Analysis

Double mutant cycle analysis (Carter et al., 1984; Hidalgo and MacKinnon, 1995) was carried out using the equation $\Omega = \frac{IC_{50}WT * IC_{50}X'Y'}{IC_{50}X' * IC_{50}Y'}$ in which Ω is the coupling factor (Hidalgo and MacKinnon, 1995) and IC_{50}WT, IC_{50}X', IC_{50}Y' and IC_{50}X'Y' are the IC_{50} values for the wild-type, each single mutant of the X-Y pair, and the double mutant, respectively. As wild type $K_{2P}2.1$ (TREK-1) is unaffected by RuR, the free energy of the interaction is zero and hence, K_a and $K_d = 1$. Coupling energy, $\Delta\Delta G_\Omega$, was calculated as $\Delta\Delta G_\Omega = RTLn\Omega$ where R = 1.987 cal mol^{-1} deg^{-1} and T = 298K.

QUANTIFICATION AND STATISTICAL ANALYSIS

As outlined in the TEVC electrophysiology methods section, each dose-response curve point is an average of at least three oocytes (n = number of oocytes, indicated in Table 1) recorded from at least two independent batches of oocytes. Specific statistical details of experiments are found in figure legends. Graphpad Prism (Version 5) was used to estimate inhibition IC_{50} values (listed in Table 1) determined by fitting a standard Hill equation with Hill coefficient fixed to -1.0. Standard error (SEM) was calculated in Prism and is indicated in figure legends and in Table 1.

DATA AND CODE AVAILABILITY

Coordinates and structures factors for the structures of $K_{2P}2.1$ I110D (PDB:6V36), $K_{2P}2.1$ I110D:RuR (PDB:6V3I), $K_{2P}2.1$ I110D:RuR:ML335 (PDB:6V37), and $K_{2P}2.1$ I110D:Ru360 (PDB:6V3C) are available from the RCSB.

Cell Chemical Biology, Volume *27*

Supplemental Information

Polynuclear Ruthenium Amines Inhibit K_{2P} Channels via a "Finger in the Dam" Mechanism

Lianne Pope, Marco Lolicato, and Daniel L. Minor Jr.

7-Feb-20

Supplementary Materials for:

‘Polynuclear ruthenium amines inhibit K_{2P} channels via a ‘finger in the dam’ mechanism’

Lianne Pope[1], Marco Lolicato[1#], and Daniel L. Minor, Jr.[1-5*]

[1]Cardiovascular Research Institute
[2]Departments of Biochemistry and Biophysics, and Cellular and Molecular Pharmacology
[3]California Institute for Quantitative Biomedical Research
[4]Kavli Institute for Fundamental Neuroscience
University of California, San Francisco, California 93858-2330 USA

[5]Molecular Biophysics and Integrated Bio-imaging Division
Lawrence Berkeley National Laboratory, Berkeley, CA 94720 USA

Lead contact: Daniel L. Minor, Jr.

*Correspondence to: daniel.minor@ucsf.edu

#Current address:
Department of Molecular Medicine
University of Pavia
Pavia ITALY

Figure S1

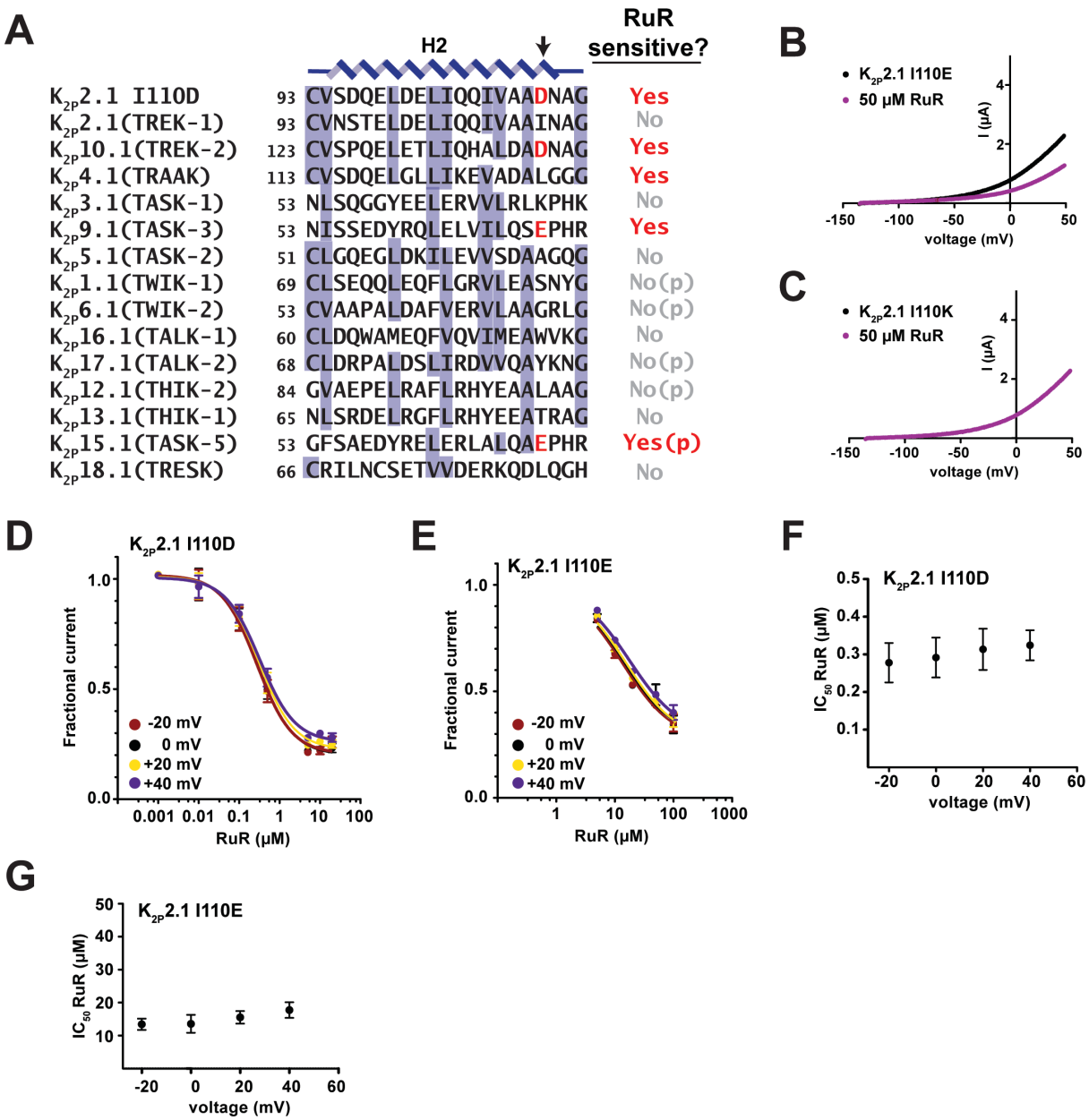

Figure S1. K_{2P} CAP sequences and K_{2P}2.1 CAP mutant functional properties, Related to Figure 1. (**A**) CAP H2 helix sequences for the indicated K_{2P} channels. Measured (Braun et al., 2015; Czirjak and Enyedi, 2003; Gonzalez et al., 2013; Musset et al., 2006) or predicted (p) Ruthenium Red (RuR) sensitivity is indicated. Arrow indicates the position of the RuR sensitivity determinant (amino acids highlighted in red). K_{2P}2.1 I110D, K_{2P}2.1 (TREK-1) AAD47569.1, K_{2P}10.1 (TREK-2) BAF83207, K_{2P}4.1 (TRAAK) AAI10328.1, K_{2P}3.1 (TASK-1) NP_002237.1, K_{2P}9.1 (TASK-3) NP_001269463.1, K_{2P}5.1 (TASK-2) NP_003731.1, K_{2P}1.1 (TWIK-1) NP_002236.1, K_{2P}6.1 (TWIK-2) NP_004814.1, K_{2P}16.1 (TALK-1) NP_001128577.1, K_{2P}17.1 (TALK-2) AAK28551.1, K_{2P}12.1 (THIK-2) NP_071338.1, K_{2P}13.1 (THIK-1) NP_071337.2, K_{2P}15.1 (TASK-5) EAW75900.1, K_{2P}18.1 (TRESK) NP_862823.1. K_{2P}15.1 (TASK-5) cannot be functionally expressed (Enyedi and Czirjak, 2010). (**B**) and (**C**) Exemplar TEVC recordings of (**B**) K_{2P}2.1 I110E and (**C**) K_{2P}2.1 I110K responses to 50 μM RuR (magenta). (**D-G**) Analysis of the voltage-dependence of RuR inhibition of K_{2P}2.1 I110D and K_{2P}2.1 I110E. (**D**) and (**E**) Dose-response curves at -20 mV (red), 0 mV (black), +20 mV (yellow), and +40 mv (purple) for (**D**) K_{2P}2.1 I110D and (**E**) K_{2P}2.1 I110E. (**F**) and (**G**) RuR IC_{50} (μM) as a function of voltage for (**D**) K_{2P}2.1 I110D and (**E**) K_{2P}2.1 I110E. Error bars are SEM.

Figure S2

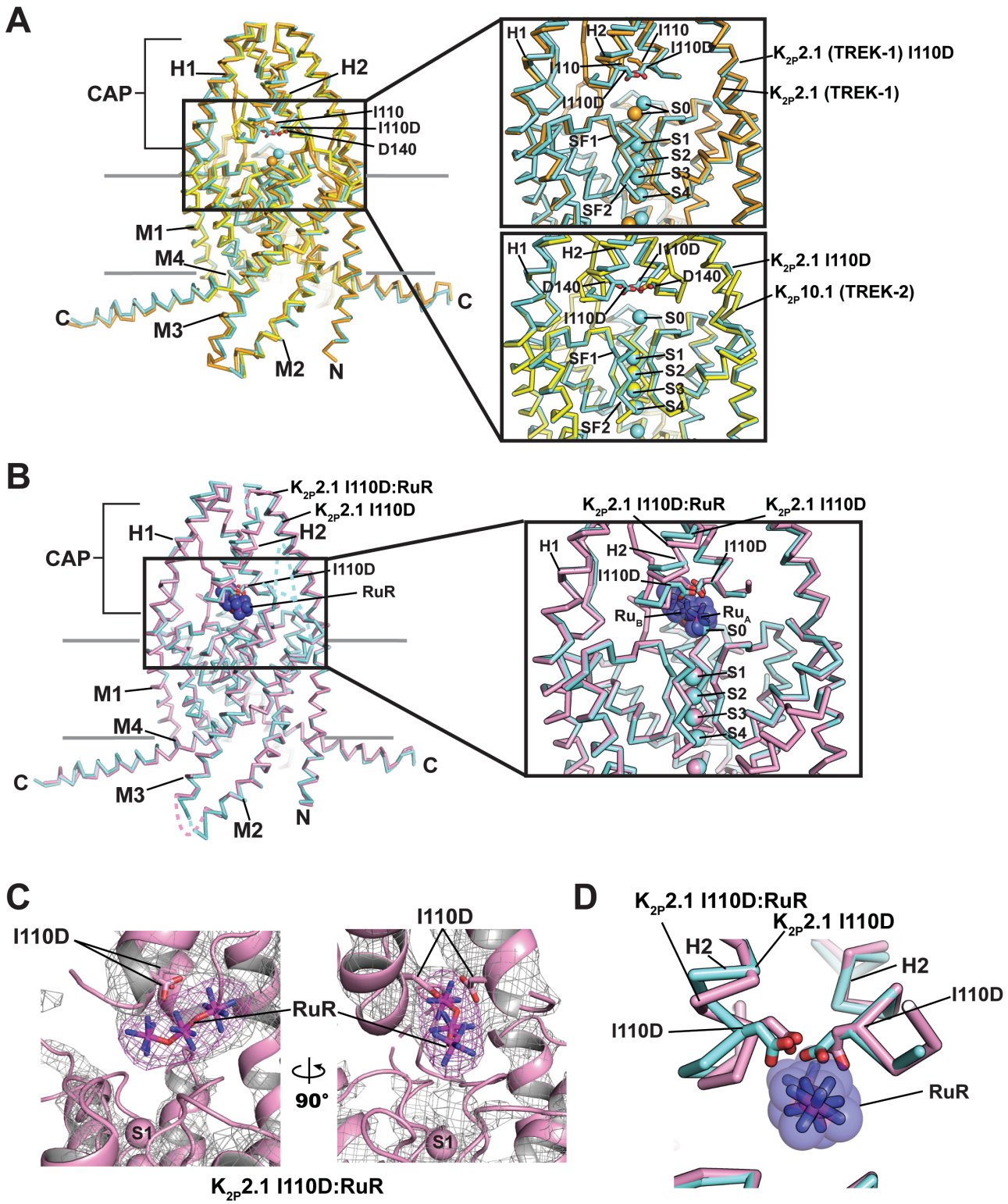

Figure S2. K_{2P}2.1 I110D structures and structure comparisons, Related to Figure 1. (**A**) Superposition of K_{2P}2.1 (TREK-1) (orange) (PDB:6CQ6)(Lolicato et al., 2017), K_{2P}2.1 I110D (cyan), and K_{2P}10.1 (TREK-2) (PDB:4BW5) (yellow)(Dong et al., 2015). Insets show comparison of area around the I110D mutation. Top, K_{2P}2.1 (TREK-1) and K_{2P}2.1 I110D; Bottom K_{2P}2.1 I110D and K_{2P}10.1 (TREK-2). (**B**) Superposition of K_{2P}2.1 I110D (cyan) and K_{2P}2.1 I110D:RuR (pink). Inset shows area around the

Keystone inhibitor site. RuR is shown as sticks with a semi-transparent surface. (**C**) Exemplar 2Fo-Fc (grey)(2σ) and Fo-Fc density (3σ)(magenta) for the K_{2P}2.1 I110D:RuR complex (pink). RuR is shown as sticks. (**D**) Close up view of K_{2P}2.1 I110D (cyan) and K_{2P}2.1 I110D:RuR (pink) showing conformational changes in the Keystone inhibitor site. RuR is shown as sticks with a semi-transparent surface.

Figure S3

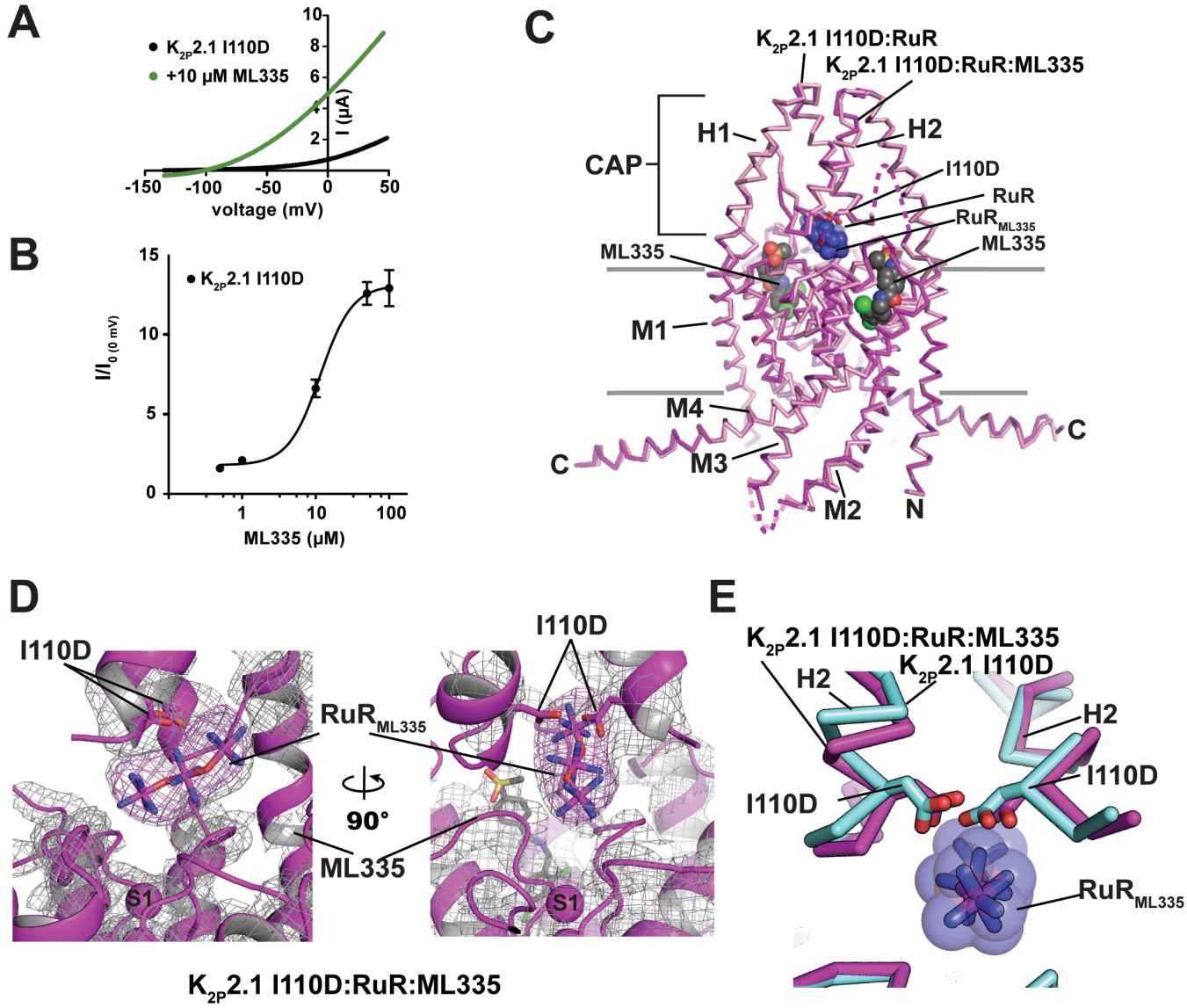

Figure S3. K_{2P}2.1 I110D ML335 response and structure of the K_{2P}2.1 I110D:RuR:ML335 complex, Related to Figure 2. (**A**) Exemplar two-electrode voltage clamp recordings of the response of K_{2P}2.1 I110D (black) to 10 µM ML335 (green). (**B**) ML335 dose-response curve for K_{2P}2.1 I110D. EC_{50} = 11.8 ± 2.3 µM, matching that of K_{2P}2.1 (TREK-1) (14.3 ± 2.7µM (Lolicato et al., 2017)). (**C**) Superposition of K_{2P}2.1 I110D:RuR (pink) and K_{2P}2.1 I110D:RuR:ML335 (magenta). I110D is shown as sticks. RuR and ML335 are shown in space filling representation. (**D**) Exemplar 2Fo-Fc (grey)(2σ) and Fo-Fc density (3σ)(magenta) for the K_{2P}2.1 I110D:RuR:ML335 complex (magenta), and (I110D, RuR, Ru360, and ML335 are shown as sticks. S1 selectivity filter ion is labeled. (**E**) Close up view of K_{2P}2.1 I110D (cyan) and K_{2P}2.1 I110D:RuR:ML335 (magenta) CAP base. Error bars are SEM.

Figure S4

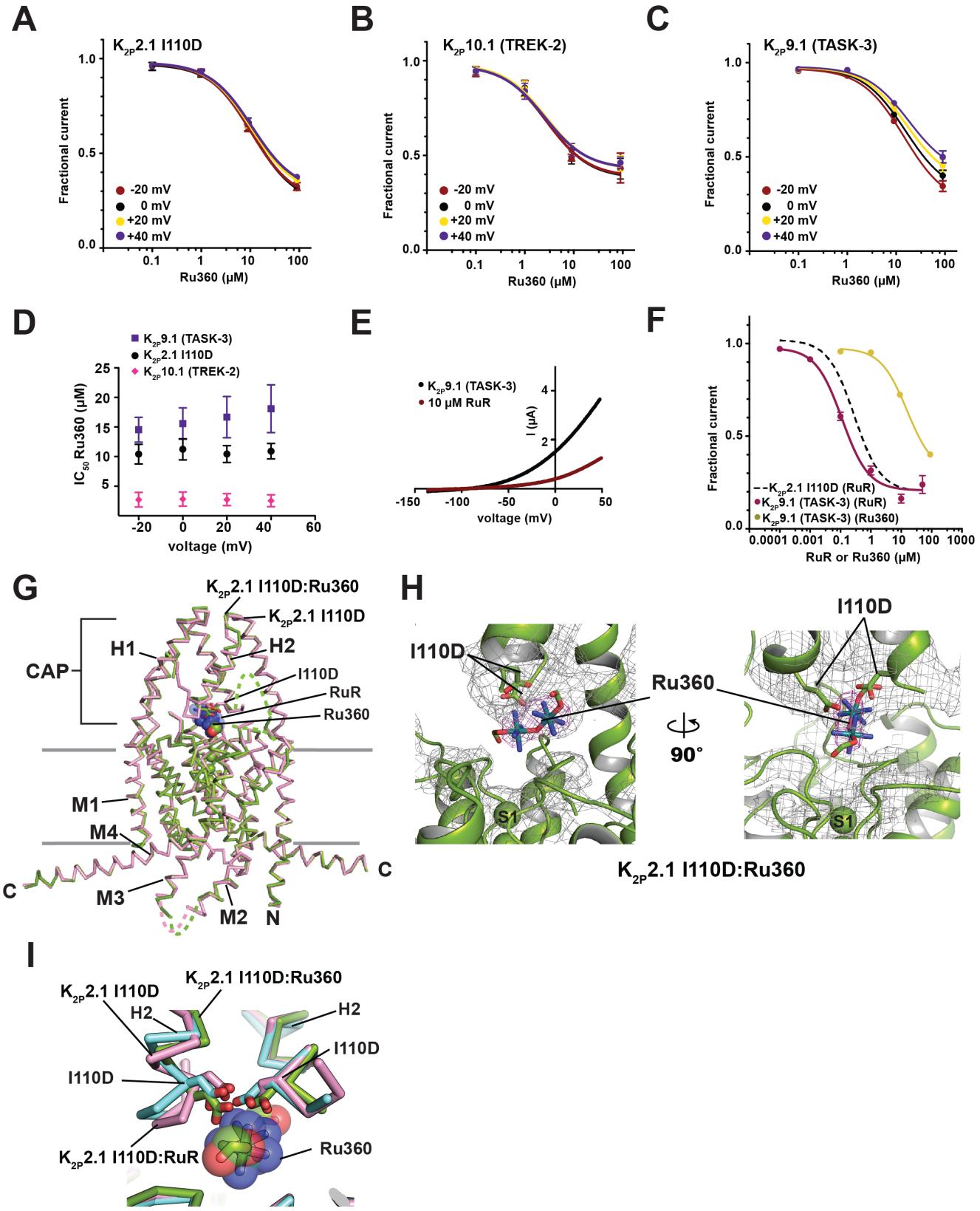

Figure S4. Ru360 inhibits K_{2P} channels, Related to Figure 3 and Table 1. (**A-C**) Ru360 dose-response curves at -20 mV (red), 0 mV (black), +20 mV (yellow), and +40 mv (purple) for (**A**) K_{2P}2.1 I110D, (**B**) K_{2P}10.1 (TREK-2), and (**C**) K_{2P}9.1 (TASK-3). (**D**) RuR IC_{50} (μM) voltage-dependence for K_{2P}2.1 I110D

(black circles), K_{2P}10.1 (TREK-2) (pink diamonds), and K_{2P}9.1 (TASK-3) (purple squares). (**E**) Exemplar TEVC recordings of K_{2P}9.1 (TASK-3) alone (black) and in the presence of 10 μM RuR (dark red). (**F**) K_{2P}9.1 (TASK-3) dose-response curves for RuR (dark red) and Ru360 (olive) (from Figure 3F). Dashed line shows RuR dose-response for K_{2P}2.1 I110D from Figure 1D. (**G**) Superposition of K_{2P}2.1 I110D:RuR (pink) and K_{2P}2.1 I110D:Ru360 (green). I110D is shown as sticks. (**H**) Exemplar 2Fo-Fc (grey)(2σ) and Fo-Fc density (3σ)(magenta) for the K_{2P}2.1 I110D:Ru360 complex (green). I110D and Ru360 are shown as sticks. S1 selectivity filter ion is labeled. (**I**) Close up view of K_{2P}2.1 I110D:Ru360 (green). K_{2P}2.1 I110D (cyan), and K_{2P}2.1 I110D:RuR (pink) CAP base. RuR and Ru360 and are shown in space filling representation. Error bars are SEM.

Figure S5

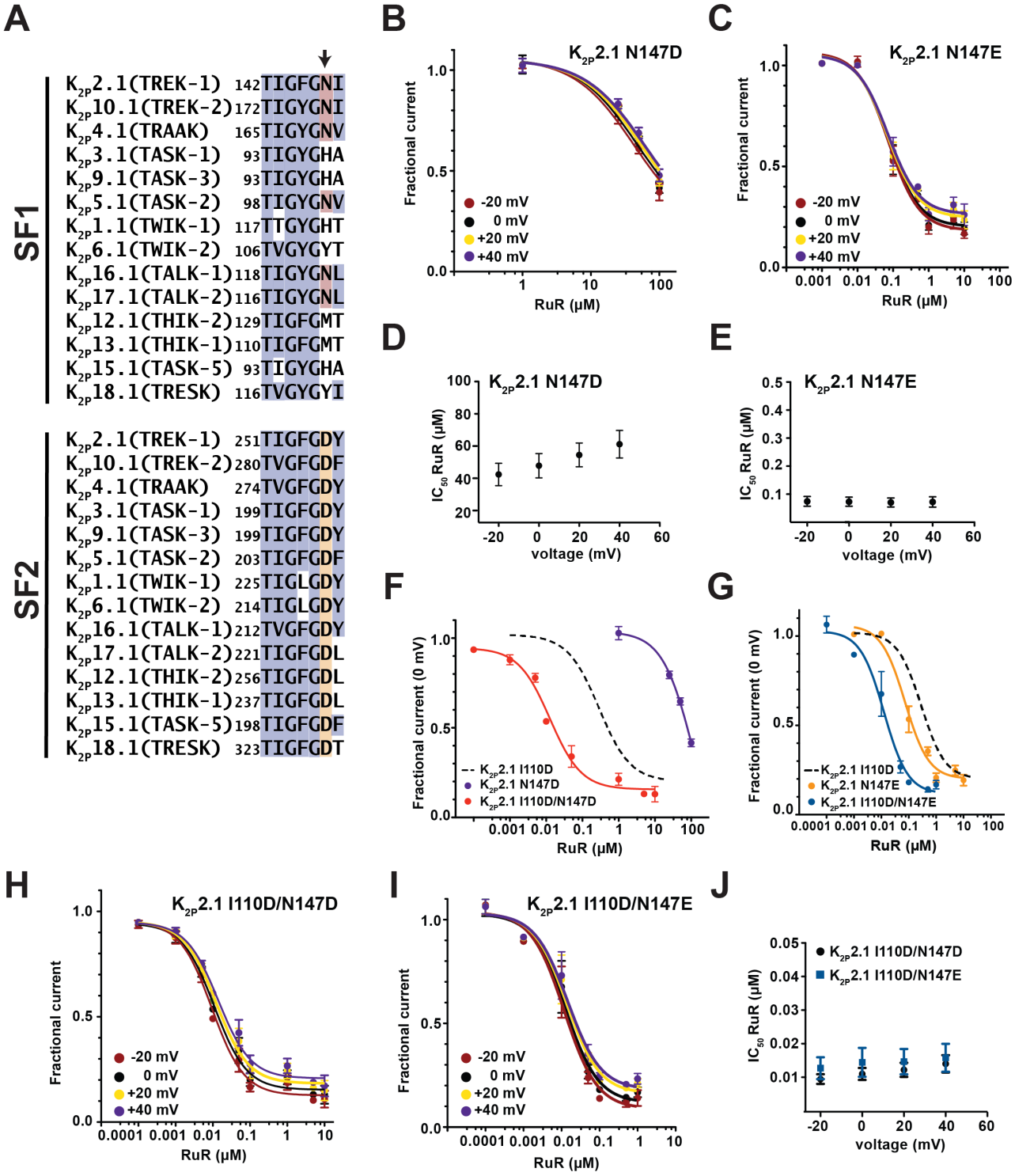

Figure S5. K_{2P} selectivity filter (SF) sequences and RuR responses of K_{2P}2.1 SF mutants, Related to Figure 4 and Table 1. (**A**) Sequence alignment of the selectivity filter 1 (SF1) and selectivity filter 2 (SF2) sequences of the following human K2P channels. K_{2P}2.1 (TREK-1) AAD47569.1, K_{2P}10.1 (TREK-2) BAF83207, K_{2P}4.1 (TRAAK) AAI10328.1, K_{2P}3.1 (TASK-1) NP_002237.1, K_{2P}9.1 (TASK-3) NP_001269463.1, K_{2P}5.1 (TASK-2) NP_003731.1, K_{2P}1.1 (TWIK-1) NP_002236.1, K_{2P}6.1 (TWIK-2) NP_004814.1, K_{2P}16.1 (TALK-1) NP_001128577.1, K_{2P}17.1 (TALK-2) AAK28551.1, K_{2P}12.1 (THIK-2) NP_071338.1, K_{2P}13.1 (THIK-1) NP_071337.2, K_{2P}15.1 (TASK-5) EAW75900.1, K_{2P}18.1 (TRESK) NP_862823.1. SF1 and SF2 sequence and numbers for K_{2P}2.1 (TREK-1)$_{cryst}$ (PDB:6CQ6)(Lolicato et al.,

2017) are identical to that of $K_{2P}2.1$ (TREK-1) AAD47569.1. (**B-C**) RuR dose-response curves at -20 mV (red), 0 mV (black), +20 mV (yellow), and +40 mv (purple) for (**B**) $K_{2P}2.1$ N147D and (**C**) $K_{2P}2.1$ N147E. (**D-E**) IC_{50} voltage dependence for (**D**) $K_{2P}2.1$ N147D and (**E**) $K_{2P}2.1$ N147E. (**F-G**) RuR dose-response curves for (**F**) $K_{2P}2.1$ N147D (purple) and $K_{2P}2.1$ I110D/N147D (red) and (**G**) $K_{2P}2.1$ I110E (orange) and $K_{2P}2.1$ I110D/N147E (blue). Dashed lines show RuR response of $K_{2P}2.1$ I110D from Figure 1D. (**H-I**) RuR dose-response curves at -20 mV (red), 0 mV (black), +20 mV (yellow), and +40 mv (purple) for (**H**) $K_{2P}2.1$ I110D/N147D and (**I**) $K_{2P}2.1$ I110D/N147E. (**J**) IC_{50} voltage dependence for $K_{2P}2.1$ I110D/N147D (black circles) and $K_{2P}2.1$ I110D/N147E (blue squares). Error bars are SEM.

Figure S6

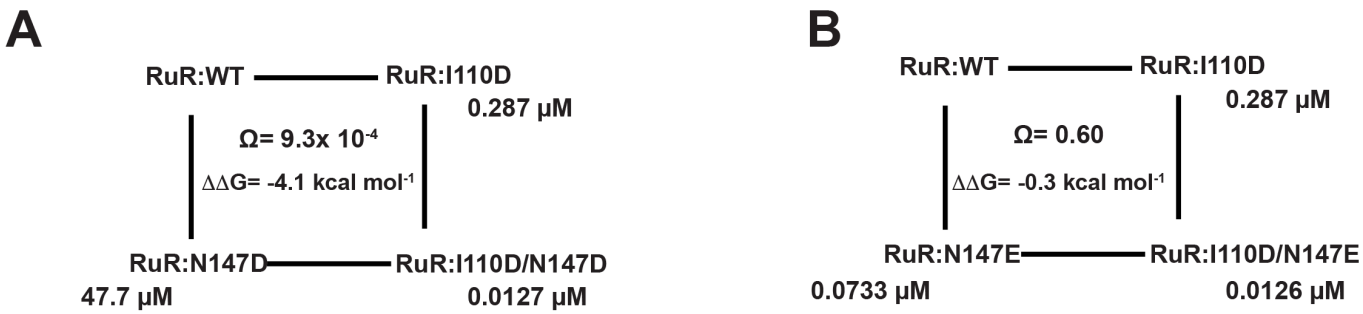

Figure S6. Double mutant cycle analysis, Related to Figure 4. Double mutant cycle analysis (Carter et al., 1984; Hidalgo and MacKinnon, 1995) for the RuR responses of (**A**) K_{2P}2.1 I110D/N147D and (**B**) K_{2P}2.1 I110D/N147E. $\Omega = \frac{IC_{50}\ X'Y'}{IC_{50}\ X' * IC_{50}\ Y'}$. as $\Delta\Delta G_{\Omega} = RTLn\Omega$ where R=1.987 cal mol^{-1} deg^{-1} and T= 298K.

Table S1. Data collection and refinement statistics, Related to Figures 1, 2, and 3.

	K_{2P}2.1 (TREK-1) I110D (PDB:6V36)	K_{2P}2.1 (TREK-1) I110D:RuR (PDB:6V3I)	K_{2P}2.1 (TREK-1) I110D:RuR:ML335 (PDB: 6V37)	K_{2P}2.1 (TREK-1) I110D:Ru360 (PDB:6V3C)
Data collection				
Space group	$P2_12_12_1$	$P2_12_12_1$	$P2_12_12_1$	$P2_12_12_1$
Cell dimensions				
a, *b*, *c* (Å)	69.19/120.40/128.35	67.95/120.3/127.82	67.02/118.74/129.04	67.74/120.71/127.27
α, β, γ (°)	90/90/90	90/90/90	90/90/90	90/90/90
Resolution (Å)	46.7 – 3.40 (3.67 - 3.40)	46.6 - 3.40 (3.66 - 3.40)	46.5 - 2.80 (2.95 - 2.80)	46.4 - 3.51 (3.85 - 3.51)
R_{merge}	0.072 (5.87)	0.090 (6.61)	0.081 (6.31)	0.110 (8.64)
$I/\sigma(I)$	9.6 (0.5)	9.1 (0.4)	13.6 (0.4)	10.8 (0.4)
$CC_{1/2}$	0.999 (0.128)	0.999 (0.138)	0.995 (0.120)	1.000 (0.149)
Completeness (%)	99.9 (100.0)	99.9 (99.9)	99.8 (98.5)	100.0 (100.0)
Redundancy	6.5 (6.7)	8.8 (8.8)	12.7 (10.0)	13.3 (13.7)
Refinement				
Resolution (Å)	15.00 - 3.40	15.00 – 3.40	14.99 – 2.80	14.98 – 3.51
No. reflections	14468	14286	24910	12595
R_{work} / R_{free}	28.6/31.8	27.5/32.8	27.1/31.6	30.2/32.5
No. atoms	4100	4192	4309	4064
Protein	4042	4092	4180	3994
Ligand/ion	55	98	127	68
K^+	6	5	5	5
Cd^{++}	3	3	3	3
Lipid	46	63	82	43
ML335	0	0	1	0
RuR	0	1	1	0
Ru360	0	0	0	1
Water	3	2	2	2
B factors				
Protein	227.94	191.96	145.60	200.63
Ligand/ion	195.40	196.35	150.32	182.87
R.M.S. deviations				
Bond lengths (Å)	0.004	0.004	0.003	0.002
Bond angles (°)	0.913	0.760	0.628	0.559
Ramachandran				
Favored (%)	94.6	93.9	92.5	96.6
Allowed (%)	4.8	5.1	6.7	3.4
Outliers (%)	0.6	1.0	0.8	0.0

Each dataset was derived from a single crystal.

[a] Values in parentheses are for highest-resolution shell.

Table S2. Structure Comparisons of RuR and Ru360 complexes, Related to Figures 1, 2, and 3.

			RMSD (Å)
K_{2P}2.1 I110D	versus	K_{2P}2.1 (TREK-1) (6CQ6)(Lolicato et al., 2017)	0.575
K_{2P}2.1 I110D		K_{2P}10.1 (TREK-2) (4BW5)(Dong et al., 2015)	0.938
K_{2P}2.1 I110D		K_{2P}2.1 I110D:RuR	0.688
K_{2P}2.1 I110D		K_{2P}2.1 I110D:Ru360	0.665
K_{2P}2.1 I110D:RuR:ML335		K_{2P}2.1 I110D:RuR	0.507
K_{2P}2.1 I110D:RuR:ML335		K_{2P}2.1 (TREK-1):ML335 (6CQ8)(Lolicato et al., 2017)	0.480
K_{2P}2.1 I110D:Ru360		K_{2P}2.1 I110D:RuR	0.561

RMSDs were calculated using Cα atoms in the specified residue ranges after optimal translational and rotational alignment of those atoms. Calculations were performed with the MDAnalysis python package version 0.19.2 (Michaud-Agrawal et al., 2011). Residue ranges include all of the α-helical portions of the structures as follows: K_{2P}2.1 (TREK-1): 45-93, 96-110, 126-190, 206-259, 268-300; K_{2P}10.1 (TREK-2): 75-123, 126-140, 156-220, 236-289, 299-331. 4BW5 comparison is for chains A and B from the asymmetric unit.